SYNTHESIS OF CARBON NANOTUBES USING METHANE-AIR PREMIXED FLAMES SEEDED WITH FERROCENE

By

ALEXANDER ZAK

A thesis submitted to the

Graduate School-New Brunswick

Rutgers, The State University of New Jersey

in partial fulfillment of the requirements

for the degree of

Master of Science

Graduate Program in Mechanical and Aerospace Engineering

written under the direction of

Professor Stephen D. Tse

and approved by

_____

_____

_____

New Brunswick, New Jersey

October 2008

ABSTRACT OF THE THESIS

Synthesis of Carbon Nanotubes Using Methane-Air Premixed Flames Seeded with Ferrocene

By ALEXANDER ZAK

Thesis Director:

Professor Stephen D. Tse

Carbon nanotubes have been extensively studied for two decades. CNTs attracted scientists' attention due to their exceptional mechanical, chemical, and electrical properties. Multiple methods including arc discharge, laser ablation, CVD, and several flame synthesis methods are used to grow CNTs. The most significant problem with all current methods is the high cost and low yield of the generated materials. Furthermore, none of the current mechanisms explain completely the formation mechanism of CNTs.

This study utilizes methane-based premixed flames to grow CNTs in a one-dimensional, stagnation point geometry. Vaporized ferrocene $Fe(C_5H_5)_2$ is seeded into the flame and acts as a catalyst for nanotube growth. CNTs are collected from the substrate located 1.5 cm away from the burner nozzle and are analyzed using TEM, SEM with EDS, and Raman spectroscopy to ascertain the presence of nanotubes.

Different carbon structures including carbon nanofibers, MWNTs, and SWNTs are generated using this technique. The presence of MWNTs is observed under TEM, while nanofibers are viewed under SEM. Raman Spectroscopy is used to identify SWNTs.

Acknowledgements

First and foremost, I would like to thank Dr. Stephen Tse for his time and guidance. His dedication and exemplary work ethic not only influenced the way I approach research, but how I will face the challenges later in life. I would also like to thank Dr Manishkuma Chhowalla and Dr. Giovanni Fanchini for their help with Raman spectroscopy. I am also very grateful to Dr. Victor Greenhut for his helpfulness and friendliness. John Petrowski deserves special mentioning, as I would not have been able to complete this work without his help and advice.

I would also like to thank my lab co-workers, Megan Smith, Cassandra D'Esposito, Dr. Geliang Sun, Dr Fusheng Xu, Xiaofei Liu, Jonathan Doyle and Hadi Halim for their friendship and support.

Finally, I want to thank my friends and family. First of all, my grandparents, who raised me. Attending graduate school would not have been possible without the sacrifices they have made for me throughout my life. Then, my mother, who always believed in me. Her support and encouragement were invaluable throughout my educational career. Finally, I thank my best friends – Artem Motvitsky and Maxim Rayetsky who have always supported me in all of my undertakings. I am also very thankful to Alexandra Walczak. Her love and friendship encouraged me throughout this work.

This work was partially supported by the National Science Foundation (Grant No. CTS-0522556) and by the Army Research Office (Grant No. W911NF-07-1-0425).

TABLE OF CONTENTS

List of Figures

List of Tables

List of Acronyms

CNT – Carbon Nanotube

SWNT – Single-Wall Nanotube

MWNT – Multi-Wall Nanotube

CVD – Chemical Vapor Deposition

TEM – Transmission Electron Microscopy

HRTEM – High Resolution Transmission Electron Microscope

SEM – Scanning Electron Microscopy

FESEM – Field Emission Scanning Electron Microscope

EDS – Electron Dispersion Spectroscopy

RBM – Radial Breathing Mode

SPIN – Numerical simulation used to calculate species, temperature and velocity profiles

Chapter 1. Introduction

1.1 Motivation

In recent years, a lot of scientific work has been performed in the field of carbon nanotubes. Most of the researchers have used arc discharge, laser ablation, and CVD methods for nanotube growth. Those that chose to use flame synthesis selected to use diffusion flame configuration. Thus, premixed flame with the use of catalytic precursor has received limited attention.

Premixed flame allows for growing CNTs in aerosol form in the flame, and depositing generated material on a cold substrate - something that can not be readily accomplished using other methods. This method could be advantageous if used to deposit nanotubes on wafers to make thin-film transistors.

1.2 Research Objectives

The objective of this work is to use a divergence stabilized methane-air premixed flame to grow CNTs and other similar nanostructures in the gas phase environment. The mechanism and optimal conditions for CNT growth are investigated.

Flame temperature, gas velocity, equivalence ratio, and catalyst particle size are varied throughout the experiment to determine the dependence of CNT formation on these factors.

1.3 Methodology

The samples are synthesized using a premixed burner primarily using methane, ethylene, nitrogen and air. The substrate located 1.5 cm beneath the burner's nozzle is used to create a one dimensional stagnation point flow. Ferrocene, $Fe(C_5H_5)_2$, acting as a catalytic precursor is introduced into the flame in order to facilitate the growth of CNTs and allow for better understanding of nanotube formation process. The samples collected onto tungsten wire are analyzed using FESEM with EDS, TEM, and Raman Spectroscopy.

1.4 Analysis Overview

This work is comprised of three major parts. Literature Overview explores the background of experimental work related to nanotubes and the importance and consequences of such research. The properties and several possible nanotube formation mechanisms are discussed. Different ways to generate CNTs, such as arc discharge, laser ablation, and flame synthesis are also summarized. Finally, this section discusses some major publications in the field of nanotube research, while drawing parallels with the current work.

The Experimental Setup section discusses in detail the premixed stagnation point flame and the setup that allows for nanotube growth. The section also contains the detailed procedure entailing all the steps necessary for successful synthesis. Numerical simulation used to estimate the chemical composition and the temperature of the flame is also briefly discussed.

Finally, Results and Discussion section presents all major research findings. Discussion of SWNTs, MWNTs and nanofibers is broken down into separate sections. Based on the results obtained using FESEM, TEM, and Raman as well as numerical simulations, possible formation routes of CNTs are discussed.

Chapter 2. Literature Review

2.1 Brief History of Carbon Nanotube Discovery

Research observations related to carbon nanotubes and nanofibers started to appear in literature as early as the end of the nineteenth century[1]. In fact, Several French scientists published their studies of carbon filaments in the late 1890s. However, the resolution of optical microscopes available at the time was so much less than that of the microscopes today, that the details and subsequent findings observed by the French are often not given too much attention. The next significant observation should be credited to Russian scientists who used TEM in 1952 to observe hollow nano-fibers[2], as seen in Fig. 1.

Figure 1 TEM Images of hollow fibers obtained in 1950 by Raushkevich and Lukyanovich using low resolution TEM[2]

The pictures they obtained clearly show a multi-wall carbon nanotube. However, the authors themselves did not foresee the importance of their discovery and did not

follow up with more detailed work. Furthermore, the fact that their work was published in the Soviet journal meant that it did not reach a wider audience outside of Eastern Europe.

The first contemporary study of CNTs, how we know them now, is most often attributed to Iijima's discoveries in the early 1990's, published in *Letters to Nature*[3]. In the publication, Iijima discusses MWNTs obtained using arc discharge method and observed under HRTEM, shown in Fig. 2. He was able to distinguish the individual walls of each nanotube, with the total diameter varying from 2 to 20 nm. Furthermore, he was able to characterize the atomic structure of nanotubes using electron diffraction.

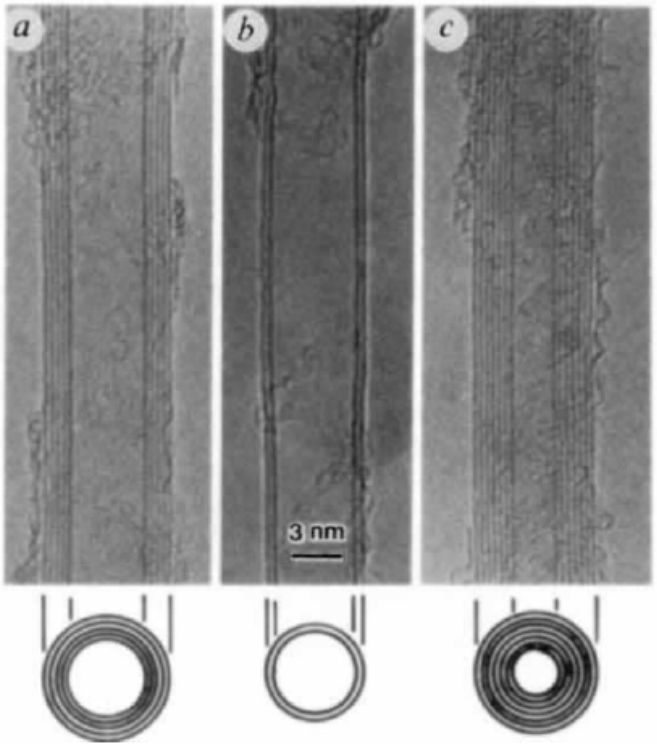

Figure 2 First TEM images of MWNTs produced by Iijima in 1992 and published in "Helical Microtubules of Graphitic Carbon"[3]

Iijima's paper had a tremendous impact on the field of nanotechnology. Hundreds of papers were published in following years detailing studies of different methods and conditions for synthesizing CNTs and focused on understanding mechanisms for their formation.

2.2 Structure of CNTs

Carbon nanotubes are essentially sheets of graphite that form a tube. SWNTs can be thought of as a single sheet of graphite, while MWNTs are multiple concentric sheets of graphite rolled into tubes of increasing diameters[4, 5]. SWNTs have diameter of around 1.4 nm. MWNTs typically consist of tens of tubes, each spaced approximately 0.34 nm from each other, with the outer diameters varying from ten to several hundred nanometers, depending on the number of walls. There are several ways how carbon atoms in the CNT bond to each other, which are described by nanotube chirality.

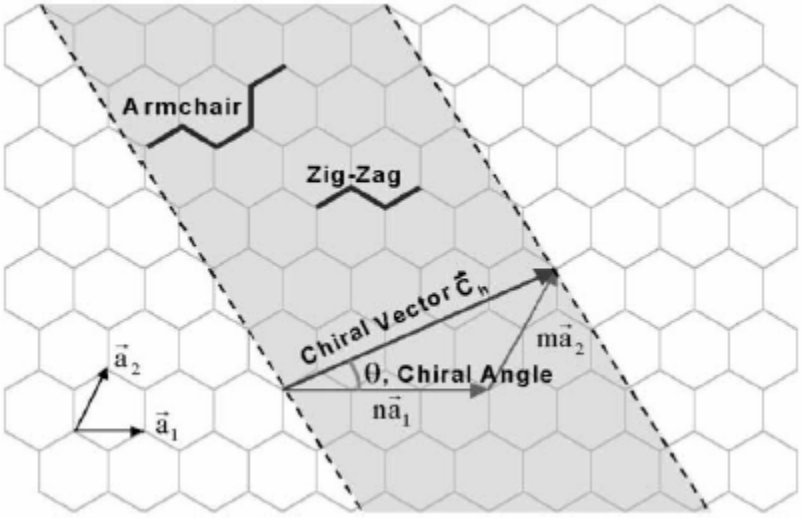

Figure 3 Chirality of CNTs[4]

As Fig. 3 illustrates, chirality is defined by $\vec{C}_h = n\vec{a}_1 + \vec{m}a_2$, where C is chiral vector, a_1 and a_2 are unit vectors; and n and m are integers. The special names given to two chiral angles of 0 and 30 degrees are armchair and zig-zag structure nanotubes. In zig-zag structure, the chiral angle is equal to zero, and hence it forms a (n,0) vector. An armchair nanotube has a chiral angle of 30 degrees and has a (n,n) vector. Figure 4 illustrates the difference between armchair and zig-zag chiralities.

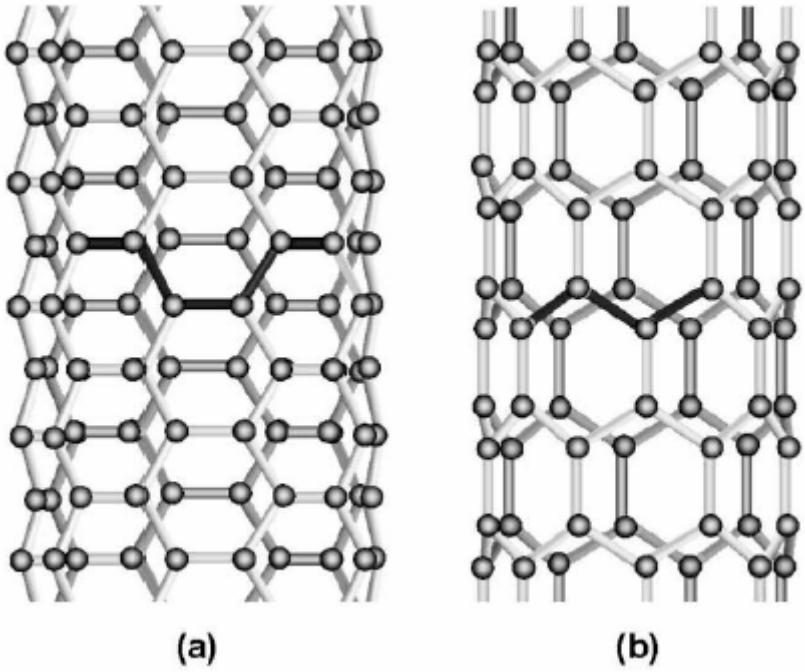

Figure 4 Two chiralities of CNTs, a) armchair and b) zig-zag[4]

A chiral nanotube is a nanotube that has a chiral angle between zero and thirty degrees.

2.3 Nanotube Properties

The structure features, such as diameter and chirality, strongly influence the properties of carbon nanotubes. The strength of nanotubes comes primarily from sp^2

covalent bonds connecting carbon atoms, resulting in a very high Young's modulus and tensile strength. For instance, Young's modulus for a single tube has been shown to reach 1 TPa, while falling to 100 GPa for bundles of CNTs[6]. Tensile strength reaches as high as 63 GPa[7, 8]. In addition to their strength, CNTs display remarkable flexibility, not breaking when bent[9, 10].

Electrical properties of CNTs can vary from conducting to semi-conducting, depending on chirality[7]. Also, electrical properties vary depending on the direction of the electron travel, with properties along the nanotube being different from the properties across its diameter. That is a peculiar property, considering that graphite sheet is a semiconductor, and CNT can be easily visualized as a graphite sheet rolled into a cylinder. Both single-wall and multi-wall nanotubes possess similar electrical properties, with the ability to carry high currents with almost no heating[11]. Thermal conductivity of CNTs is shown to exceed that of graphite, and for multi-wall nanotubes it approaches 3000 W/K[12]. As with its electrical properties, thermal properties of nanotube are anisotropic.

Multiple future applications for CNTs are expected in the fields of high strength composite materials, where nanotubes would be beneficial due to their low density and high aspect ratio. Various types of electronics such as sensors and LEDs replacements and even hydrogen storage for fuel cells[11, 13, 14] are under development.

2.4 Nanotube Formation Mechanisms

The mechanism for CNT formation is not completely understood at this time. However, several criteria that need to be satisfied in order for the nanotube to form have

been identified. Depending on the method, high temperature, abundance of CO[46], and enough residence time can all be critical for successful nanotube formation.

Several models are proposed that explain CNT formation in more detail. The first one is Yarmulke mechanism, translated from Yiddish as a "skullcap". This mechanism is based on the metallic catalytic particle removing hydrogen atoms from hydrocarbons available in the flow field, and causing freed carbon to diffuse along the length and becoming attached to the open edges of the forming nanotube[15]. The shape of the "cap" comes from the fact that newly-arriving carbon atoms form the carbon sheet that follows the spherical shape of the catalyst particle[16, 17]. In this mechanism, the diameter of the nanotube is governed by the size of the catalyst particle, which explains the often found correlation between particle size and CNT diameter in the literature[18, 19]. It has been furthermore observed by Vander Wal and Hall[18] that Fe catalytic particles formed SWNTs when they were about 1 nm in diameter, while catalyst particles from 1 to 10 nm form MWNTs.

This growth mechanism predicts there are three ways in which new carbon atoms can attach themselves to the existing structure. First, carbon can form a complete sphere around the catalyst, thus deactivating it. In fact, unless the conditions for CNT growth are optimal, that is the most likely scenario[17]. Another possibility is a formation of a second 'cap' above the first one surrounding the catalyst. Formation of the second and concurrent 'caps' allows for more layers of carbon to form, thus resulting in the growth of multi-wall nanotubes. And finally, the carbon atom can lengthen the nanotube, by inserting itself between the growing end and a catalyst particle. For that to happen, the

catalyst particle should be just the right size, so that it does not tend to over-coat due to its curvature.

Another mechanism for CNT formation is based on carbon atom diffusion due to temperature gradient at the catalyst particle[20, 21]. According to the model, carbon starts settling on one side of the particle, preventing heat exchange with the surroundings which results in the temperature gradient. At this point, carbon blanketing the catalyst is often amorphous carbon. Another result is the pear-like shape that the catalyst particle starts to take. The newly diffused carbon particles start to attach themselves to other carbons further away from the catalyst and eventually drive the catalyst away from the substrate on which the catalyst initially resides, as shown in Fig. 5. As the catalyst separates from the substrate which acts as a heat sink, the diffusion rate increases and the CNT growth accelerates. The limiting factor for the length that the CNT can reach is based on the radiation and conduction losses. As diffused carbon has to travel further and further away from the original catalyst, the temperature gradient becomes less and eventually longitudinal growth stops. Alternatively, if the catalyst particle does not get separated from the support fast enough, then the diffused carbon coats the catalyst instead of growing into CNT. Once the catalyst is over-coated with carbon it becomes deactivated.

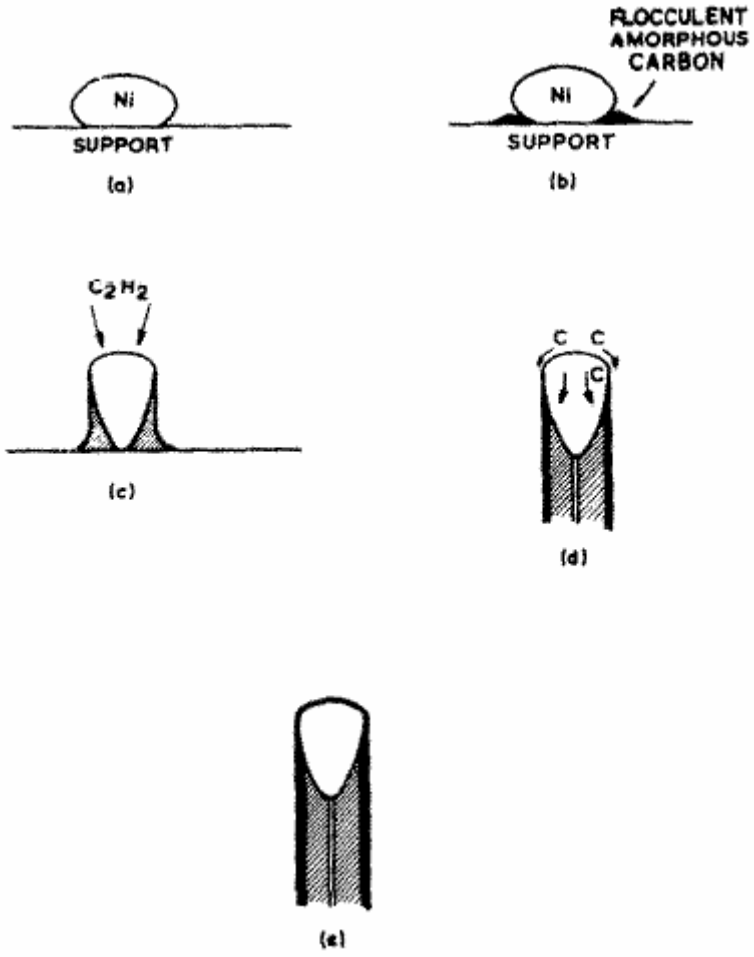

Figure 5 Illustration of Baker Mechanism[20]

The Baker mechanism discussed just now is an example of a tip-growth CNT model, where the catalyst particle remains at the leading edge of a growing nanotube[22]. The same mechanism is also referred to as carbon salvation, diffusion and precipitation growth mechanism[18, 19].

2.5 Synthesis Methods for Carbon Nanotubes

The first method is arc discharge. That is the method Iijima used for his experiments when he observed the first CNTs. Current is passed through two carbon-rich

electrodes separated by a short distance that is filled with an inert gas. The chamber where the setup is located is usually held at below-atmospheric pressure, although exact pressures vary from one experimental setup to another[7]. Helium, argon and hydrogen[1, 23], and even liquid nitrogen[24] are the gases used the most often. An electric discharge occurs between anode and cathode, and SWNTs or MWNTs form on the walls of the setup enclosure and the cathode, as the precursor and the carbon forming a layer on the anode are vaporized. The inert gas that fills the chamber and the presence of the metallic precursor in the anode are what governs if SWNTs or MWNTs are created. Interestingly, some researchers used a non-metallic anode with grooves filled with precursor and carbon mixture and reported successful generation of CNTs[23].

The advantage presented by this method is the fact that large quantities of CNTs can be generated in the relatively simple setup. However, the downside to the method is the amount of impurities that usually contaminate CNTs, especially SWNTs[7]. The control over the CNT parameters can be achieved by varying anode to cathode distance, inert gas composition, pressure, amount and type of the catalyst, application of the magnetic field, and plasma rotating arc discharge[25]. Modification to these parameters influences what type of CNTs would be generated, how much impurities would be mixed in with the CNTs, and what structure the CNTs would have.

The second method closely related to arc discharge is laser ablation, (Fig. 6), but it is thought to give a more homogeneous product yield[26]. The difference between the two methods is that carbon rich graphite is vaporized by a laser. Afterwards, formed structures are collected on the copper plate, to which they are carried by the inert gas flow. As the gaseous elements such as carbon particles cool, they form fullerene

molecules and grow into nanotubes[27]. This method is mostly conducive to SWNTs formation, even though MWNTs were also reported.

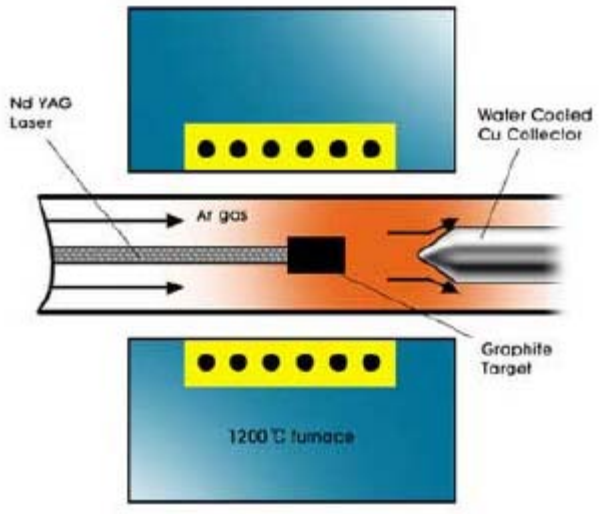

Figure 6 Schematic of Laser Ablation Setup[7]

Another method very often used to generate CNTs is Chemical Vapor Deposition (CVD) that is illustrated in Fig. 7. The major premise of this method is supplying energy to the gaseous carbon molecules, which results in CNT growth. The catalyst carbon is usually placed on the substrate via sputtering and annealing prior to synthesis. Energy transfer during synthesis can usually be facilitated by heating of the substrate. An alternative method, plasma enhanced CVD, uses anode and cathode, with substrate acting as one of them. When voltage is applied between the electrodes, the discharged current passes through the catalyst carbon and carbon-rich gas often used to improve CNT synthesis. Ferrocene, as well as xylene[28, 29], can be used in CVD to facilitate the formation of MWNTs.

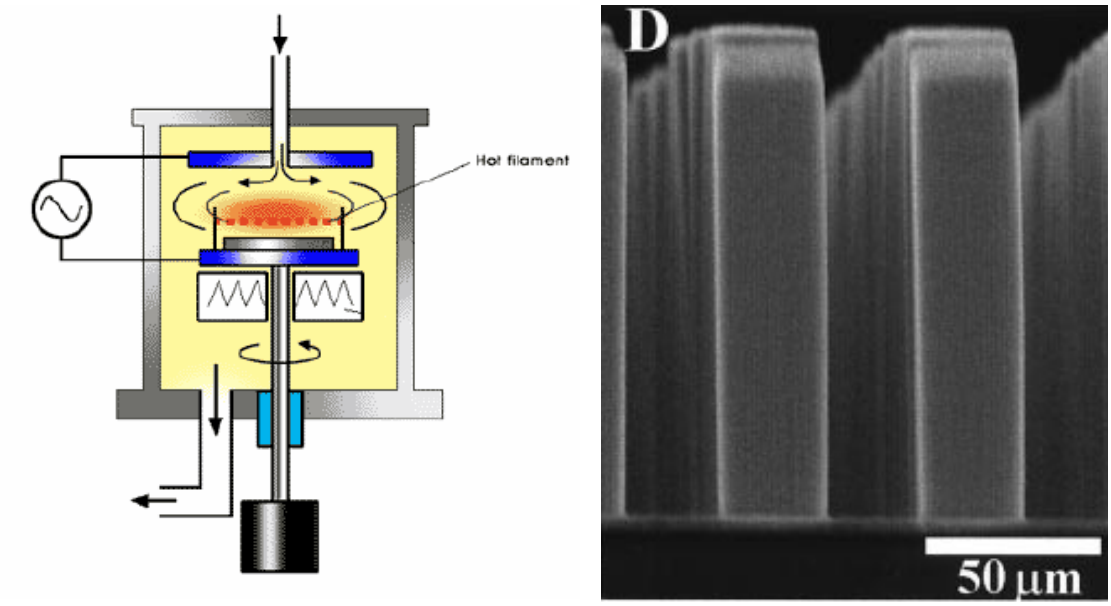

Figure 7 Schematic of Plasma Enhanced CVD[7] and an example of well-aligned CNTs obtained using CVD[30]

The advantages that the CVD method of CNT growth presents are the scalability and large volume of CNTs generated. CVD also allows material deposition on the surfaces of various shapes[31], which can prove advantageous in certain nanotube applications, while allowing for wide variation of stoichiometry. Extremely well-aligned growth of CNTs can also be achieved when using patterned silicon surfaces[30], as Fig 7 illustrates. The downside to the method is the lack of controls over CNT parameters that other methods have.

2.6 Flame Synthesis

The method of interest in this thesis is flame-based CNT synthesis. This method has received less attention compared to CVD and arc discharge, but presents several key advantages, such as cost effectiveness and scalability[32]. Synthesis of CNTs can be

obtained using diffusion, premixed, and pyrolysis flames. The flame can be seeded with CNT catalyst precursors or unseeded. The experimental conditions for CNT generation can be precisely controlled, via flame temperature, velocity, and species concentration. This in turn facilitates the understanding of the exact pathways that CNTs follow in their growth. Furthermore, flame synthesis is a very efficient process, as fuel serves both as the source of energy as well as a reactant necessary for CNT growth[33].

2.6.1 Diffusion Flames

A diffusion flame is a flame in which oxidizer and fuel species are initially separated and mix through diffusion. In a normal co-flow diffusion flame, the inner and outer diameter channels of the burner carry oxidizer and fuel separately, with the fuel being delivered through the inner tube. In an inverse diffusion co-flow flame, the oxidizer flows thought the middle tube, while fuel gets routed through the outside tube. In the counter flow diffusion flame, burners are positioned vertically so that the burner nozzles are opposite to each other. One burner exclusively carries an oxidizer, and the second burner delivers fuel. The advantage presented by such flame is that it eliminates strong gradients in temperature, species concentration, and velocity in both radial and axial directions that are usually present in co-flow diffusion flame. Instead, counter-flow setup allows for a quasi-uniform one-dimensional flame with eliminated gradients in vertical direction[34]. Furthermore, several numerical computational models are available to simulate the combustion in counter-flow flames. All three different setups are shown in Fig. 8.

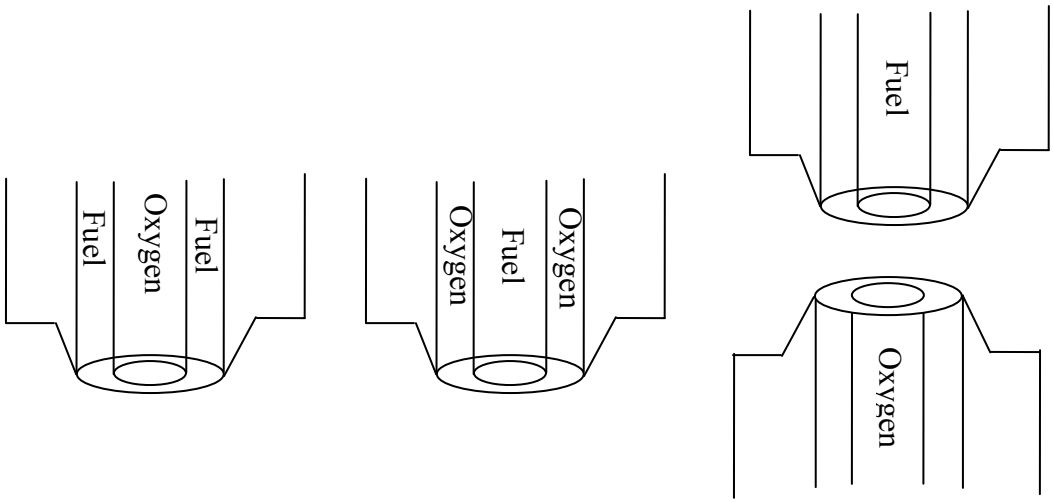

Figure 8 Inverse, Normal and Counter-flow Diffusion Burner Setups

Yuan *et al*[35, 36, 37] employed a normal co-flow diffusion flame using unseeded methane-air mixture to successfully generate MWNTs that were 10-60 nm in diameter, collecting samples on Ni-Cr-Fe grid placed into the flame. Wander Val, on the other hand, utilized the supported catalyst method in an acetylene/ethylene normal co-flow diffusion flame. A plate acting as a substrate and coated with a mixture of powder TiO_2 and metal nitrate was inserted into the flame to obtain a significant yield of MWNTs ranging from 10 to 100 nm in diameter[38].

Lee *et al*[39] used an ethylene inverse diffusion flame, but employed a nickel catalyzed substrate that was placed inside the flame. The observed MWNTs were 20 to 60 nm in diameter while the temperature was maintained between 900 and 1400 K. Nanofibers were formed outside of that temperature window.

Kennedy[34] and Merchan-Merchan *et al*[40] used counter-flow ethylene- and methane-air diffusion flames with and without catalyst to generate MWNTs. The later experiment without catalysts showed MWNTs with several walls mixed in with soot and nanoparticles. When using Ni, Cu, and Fe catalysts, the diameter of obtained MWNTs increased to 20 to 100 nm, with much higher yield and less amorphous structures.

In fact, images obtained by Merchan – Merchan[40] resemble the images obtained in this work (discussed later), despite the fact that Merchan – Merchan used counter–flow burner and no catalyst. The fuel used in the experiment was CH_4, while N_2 was used as a co-flow gas. The yield of obtained MWNTs shown in Fig. 9 was significant, but they were clearly over-coated with carbon.

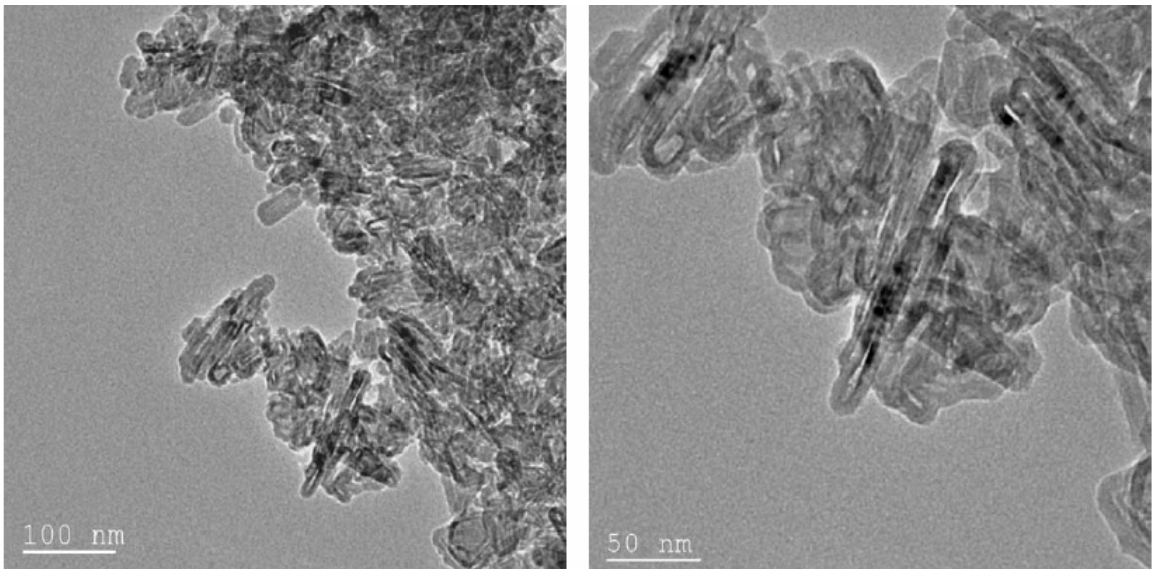

Figure 9 Images of CNT agglomerates obtained under TEM[40]

Diener *et al*[41] used a diffusion flame in a low pressure combustion chamber with iron and nickel acting as catalysts to generate SWNTs using ethylene and acetylene and MWNTs using benzene as fuel.

2.6.2 Premixed Flames

The defining characteristic of a premixed flame is the fact that fuel and oxidizer are mixed together before combustion occurs. There are also very well known formulae for flame speed and adiabatic flame temperature, which allow for better understanding of the flame environment. Finally, numeric algorithms such as PREMIX[69] allow for simulating one dimensional flame and processes that govern its formation.

In 1994, Duan and McKinnon[42] used rich benzene-air premixed flame at low pressure and were able to observe MWNTs randomly distributed in the soot. The unfortunate observation they made was the inconsistency of the yield of the soot – some samples were dominated by CNTs while others were predominantly amorphous soot, which made quantification of the results problematic.

In 1995 Chowdhury *et al*[43] used benzene, acetylene, or ethylene in a premixed flame at low pressure. The samples that they collected on the probe within the flame at about 2000 K revealed the presence of various fullerene nanoparticles and some MWNTs.

An interesting comparative study was conducted in 2002 by Goel *et al*[44]. Using benzene and oxygen flames, they were able to compare CNT yield from both diffusion and premixed flames and found that diffusion flames are more favorable for CNT formation. Furthermore, CNTs were only observed in the premixed flame when residence time was increased considerably higher than that of a diffusion flame counterpart.

Height *et al*[32] utilized an acetylene flame with vaporized $Fe(CO)_5$ acting as a catalyst precursor to generate SWNTs. Nanotubes were collected using a thermophoretic sampling probe at various positions above the flame at equivalence ratios ranging from

1.5 to 1.9 and flame temperatures from 1500 to 1800 K. It was found that discrete carbon particles were dominant at the lower equivalence ratios, while soot began to contaminate CNT yield closer to Φ=1.9.

Vander Wal *et al* investigated what fuels are the most conducive to CNT formation[45]. Cobalt catalyst was deposited onto a substrate that was inserted into post-flame gases estimated to be at 800 C, where CNTs were expected to grow. They found that at equivalence ratios from 1.5 to 2, using methane as a fuel did not yield any carbon based formations, while using ethane, ethylene, acetylene, and propane yielded significant amounts of MWNTs and nanofibers.

Vander Wal[46] utilized a pyrolysis flame with and without metallic catalysts to obtain single- and multi-wall carbon nanotubes. In the pyrolysis flame, the catalyst precursor aerosol is supplied through the metal tube inside of the flame, where there is no combustion. Due to the lack of oxygen, the combustion does not take place inside of the tube, but there is enough heat supplied by the reaction outside of the tube as for reactions necessary for nanotube formation to take place. In some cases, acetylene flame with Fe and Ni[46, 47, 48] catalysts were used to obtain a significant yield of SWNTs[46, 47, 49] and MWNTs[47]. Based on the obtained results, it was found that the size of the metal catalyst directly influenced the size of the CNT. In fact, as the diameter of the catalyst particle increased, the yield of SWNTs decreased while their length became shorter[46]. Another interesting observation was that temperature played a negligible role in CNT growth from Fe particles. Despite these observations, Vander Wal and Ticich[50] also found that a catalyst particle can initially be larger than subsequent CNT. However, for that to happen the particle would have to be broken up in the flame so that the smaller fragments of

catalyst can facilitate CNT growth. Figure 10 illustrates several obtained MWNTs that appear to be over-coated with carbon.

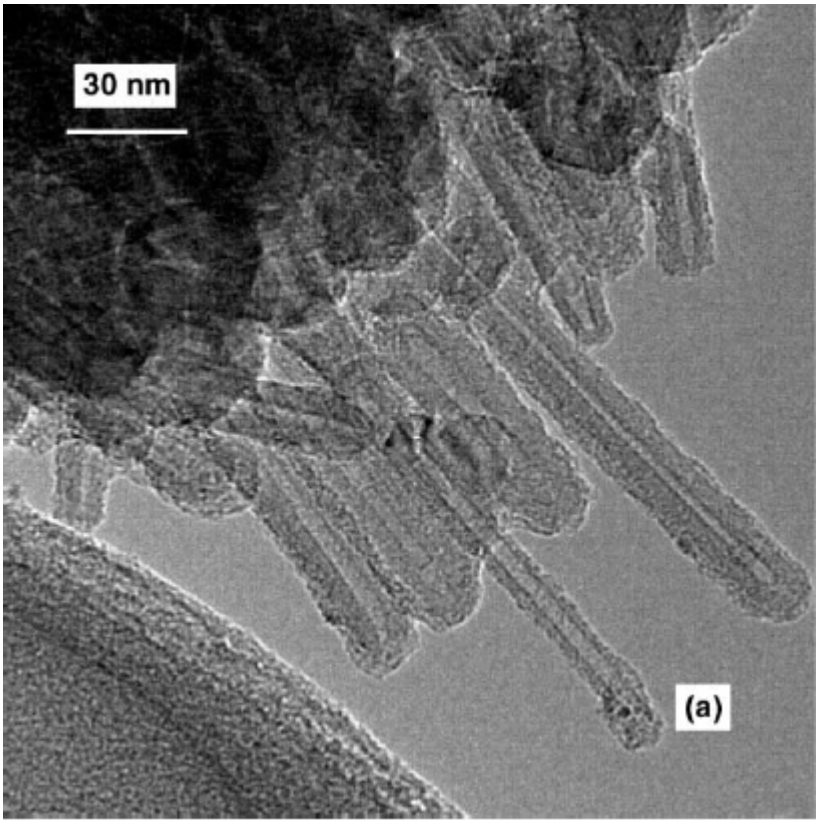

Figure 10 MWNTs obtained by Vander Wal and Ticich[50] using pyrolysis flame

Another observation made was that the increase of CO resulted in the increased encapsulation of CNTs by amorphous carbon. It was also observed that Fe acting as a catalyst leads to higher subsequent CNT yield than Ni catalyst. A further study suggested that Fe catalyst might be more appropriate for SWNT growth, while Ni catalyst is better used for nanofiber growth[18]. The author suggested that Fe particles are catalytically active at smaller diameters than Ni, thus resulting in the growth of smaller diameter structures, such as SWNTs.

A study by Murr *et al*[51] looked at CNTs generated in the ambient air by common fuel-gas combustion sources, such as a gas stove. The nanotubes generated in this study are shown in Fig. 11. Fuels examined included methane and propane. Surprisingly enough, samples collected directly above the flame onto TEM grids revealed collections of CNTs and amorphous carbon. These findings indicate that CNTs might grow under a variety of conditions that might not have to be meticulously controlled. The images obtained by this group strongly resemble the images obtained in this work (to be discussed in a later section).

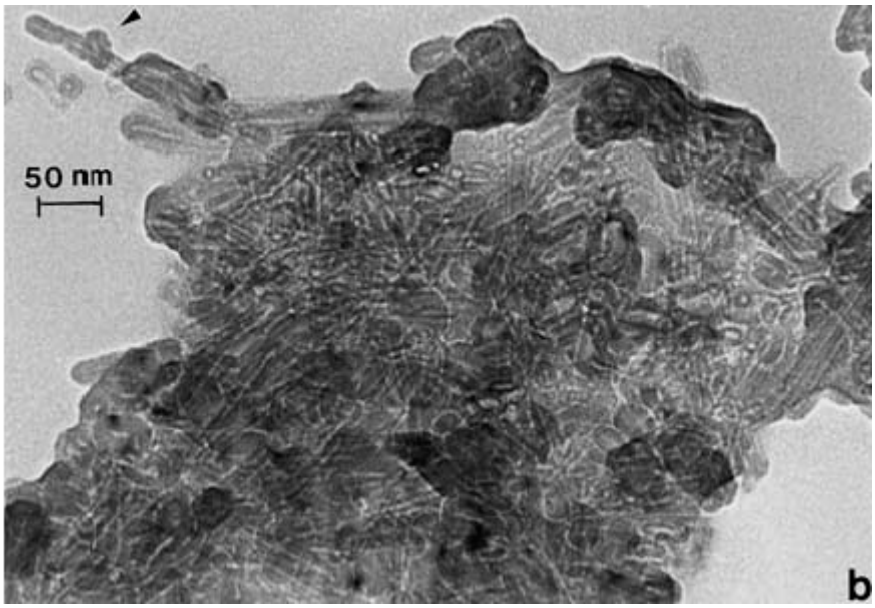

Figure 11 Bright-field TEM image of CNTs[51]

Zhao *et al*[52], used a premixed ethylene flame to synthesize TiO_2 nanoparticles instead of CNTs. However, the stagnation point flame method used by Zhao is of great interest in CNT research. The advantage presented by the stagnation flame is the significant control over residence time and making the premixed flame increasingly one-dimensional.

2.6.3 Laminar Flow Reactor

Another interesting way for synthesizing nanoparticles and SWNTs was introduced by Nasibulin and Moisala[53, 54]. Their group used a laminar flow reactor, shown in Fig. 12, which is somewhat similar to the pyrolysis flame setup used by Vander Wal[46, 47, 49]. The ceramic tube was inserted into the reactor that carried CO, while another smaller diameter ceramic tube encapsulated a hot wire generator used to vaporize precursor metal catalyst. Using ferrocene as the catalyst precursor in the aerosol synthesis method, a significant yield of SWNTs was collected right from the synthesis gas phase region.

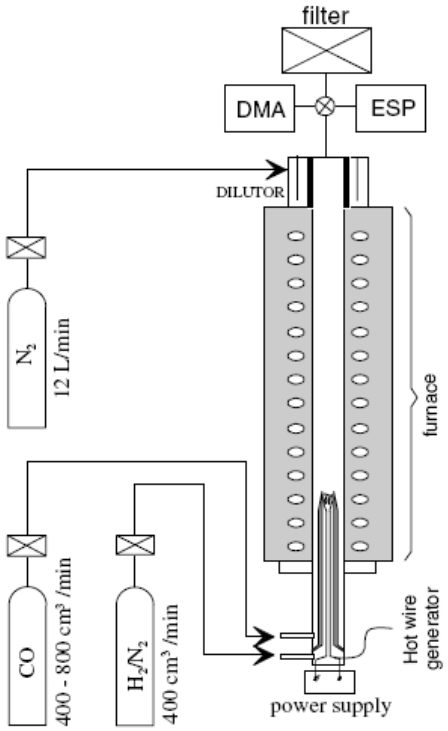

Figure 12 A Laminar Flow Reactor used by Moisala and Nasibulin[53, 54]

An interesting observation related to the research discussed in this thesis was noted by Nasibulin *et al*[55]. While using a laminar flow reactor to generate CNTs, they were able to synthesize CNTs that were later viewed under TEM. The picture obtained (Fig.

13) bears striking similarity to the images obtained in this work (to be discussed later). At high magnification, the metallic catalyst is shown to be over-coated by carbon atoms, but CNTs are not present. The explanation given is the fact that all SWNTs were quickly destroyed due to electron bombardment in TEM.

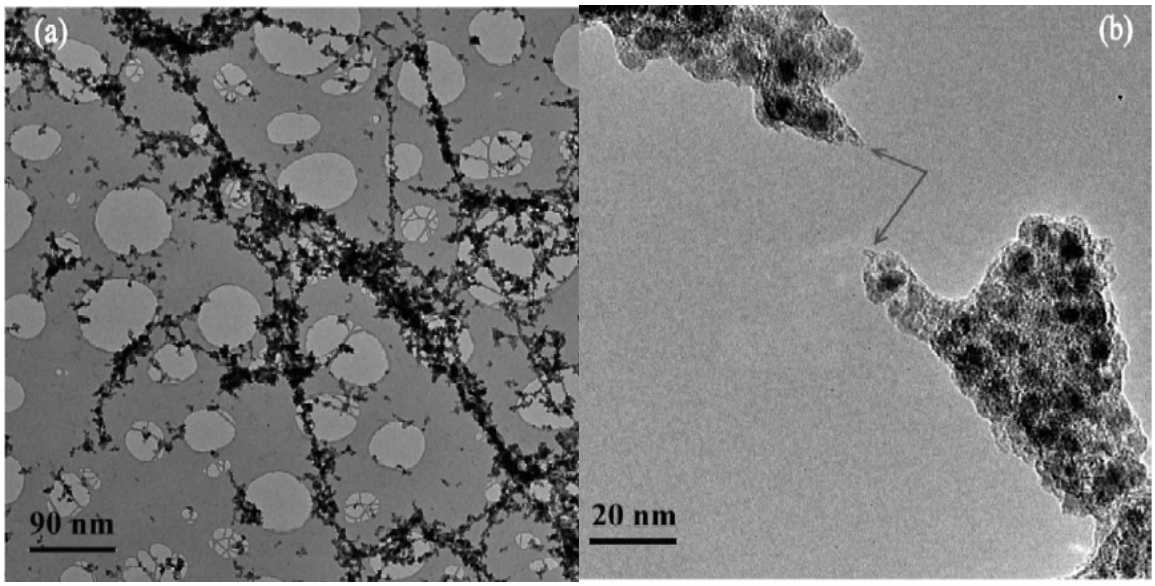

Figure 13 Images of metal catalyst and amorphous carbon at low and high magnification showing possible destruction of SWNTs due to electron damage under high magnification[55]

Chapter 3. Experimental Setup

3.1 Burner and Substrate Setup

Experimental setup for this experiment consists of a brass co-flow jet burner and a copper-aluminum substrate located 1.5 cm beneath the nozzle of the burner. The burner and the substrate are illustrated in Fig. 14. Both the burner and the substrate are actively water-cooled during the experiment. The setup is encased by an acrylic enclosure with an exhaust hood in order to minimize possible flame disturbances, as well as to provide a route for the escape of product gases from by the flame.

The burner is specifically designed to accommodate a premixed flame. Methane, air, and nitrogen are introduced into the mixing chamber of the burner. At the exit, co-flow nitrogen prevents outside air from reaching the flame which allows precise monitoring of the composition of the reacting gases, without having to take into account oxygen from the ambient air. The flow of each gas is controlled via mass flow controllers.

The substrate is primarily machined out of aluminum with channels running through to allow for effective cooling. The top of the aluminum substrate is covered by the thin copper sheet with thermal paste in between to provide for better heat dissipation. The temperature of the substrate is one of the most important factors in this experiment, since CNTs can grow at the substrate if the temperature is high enough. Being that the purpose of the experiment is to generate CNTs in the aerosol, CNT growth on the substrate is not intended.

To make sure that the substrate always remains below 100° C, the cooling water temperature is regulated using an electric cooler. It is necessary to constantly monitor the

surface of the substrate to make sure that it is always at the point where if temperature of the substrate was lowered just a bit then water condensation would start. However, condensation needs to be avoided, as CNTs are collected off the surface of the substrate.

Both tap water and water passing through the cooler were attempted to be used for burner and substrate cooler interchangeably. Either configuration allows running of the experiment; however water passing through the cooler allows regulating the temperature more precisely, which is needed for the burner, but more so for the substrate.

The main consideration when cooling the burner is to keep it as cool as not too allow brass, which the burner is made out of, to melt. The melting temperature of the brass is 930° C, and thus it is relatively easy to prevent the burner from reaching this temperature. However, another issue is reducing the condensation on the burner surface that occurs whenever cooling water temperature is lower than the temperature of the ambient air. Clearly when using the electric cooler unit to cool the burner the temperature can be set just slightly higher than ambient, which prevents condensation. Tap water however is usually colder than ambient temperature. To minimize condensation, a needle valve is installed on the line and is manually adjusted so that the temperature of the burner stays between 25 to 30 degrees centigrade. If the temperature is lower, condensate drips down on the substrate compromising sample collection and extinguishing the flame. Also, at 30 degrees Celsius the burner is cold enough as to prevent the flame from flashing back, which helps to stabilize the flame.

The location of the substrate is chosen to be 1.5 cm away from the burner to insure a stagnation flow, which could theoretically be modeled using PREMIX and SPIN[70] flame simulations. Alternative substrate locations up to 4 cm away from the

burner nozzle have also been tried but caused several problems. Stagnation point flow is easier to achieve at low separation distances, while SPIN simulation would not converge if the flow was not stagnant.

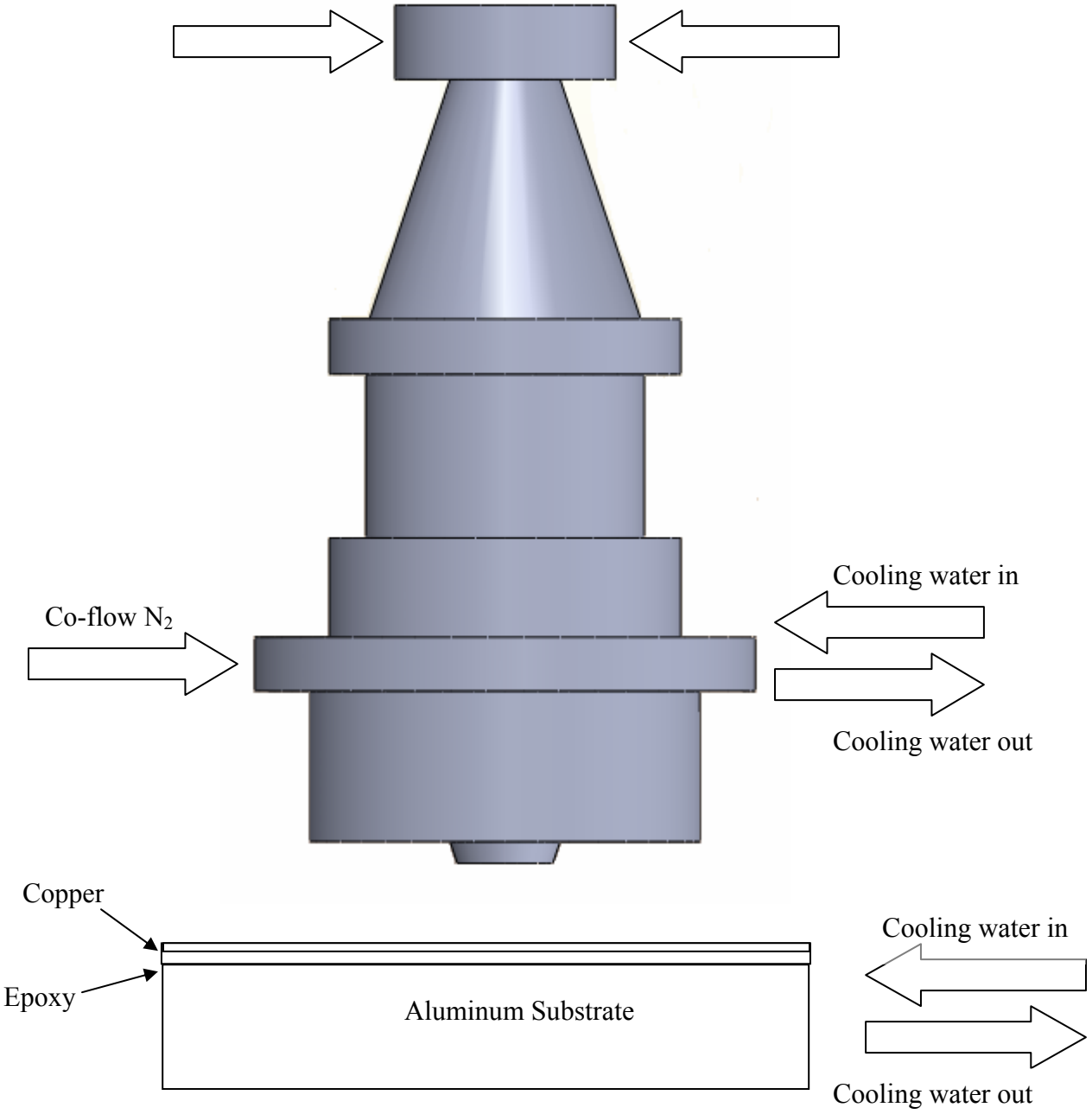

Figure 14 Schematic drawing of the burner used in the experiment

The ferrocene feeder is actively cooled as well during the experiment shutdown. As the experiment is completed, the temperature controller is turned off. However it takes at least an hour for the feeder temperature to go below 100° C. During that time, the experiment has to run, as to prevent ferrocene accumulation in the lines. Active cooling of the feeder using tap water expedites cooling process, and allows the feeder to reach an acceptable temperature within 15 to 20 minutes.

The main components of the experimental system are depicted in Fig. 15.

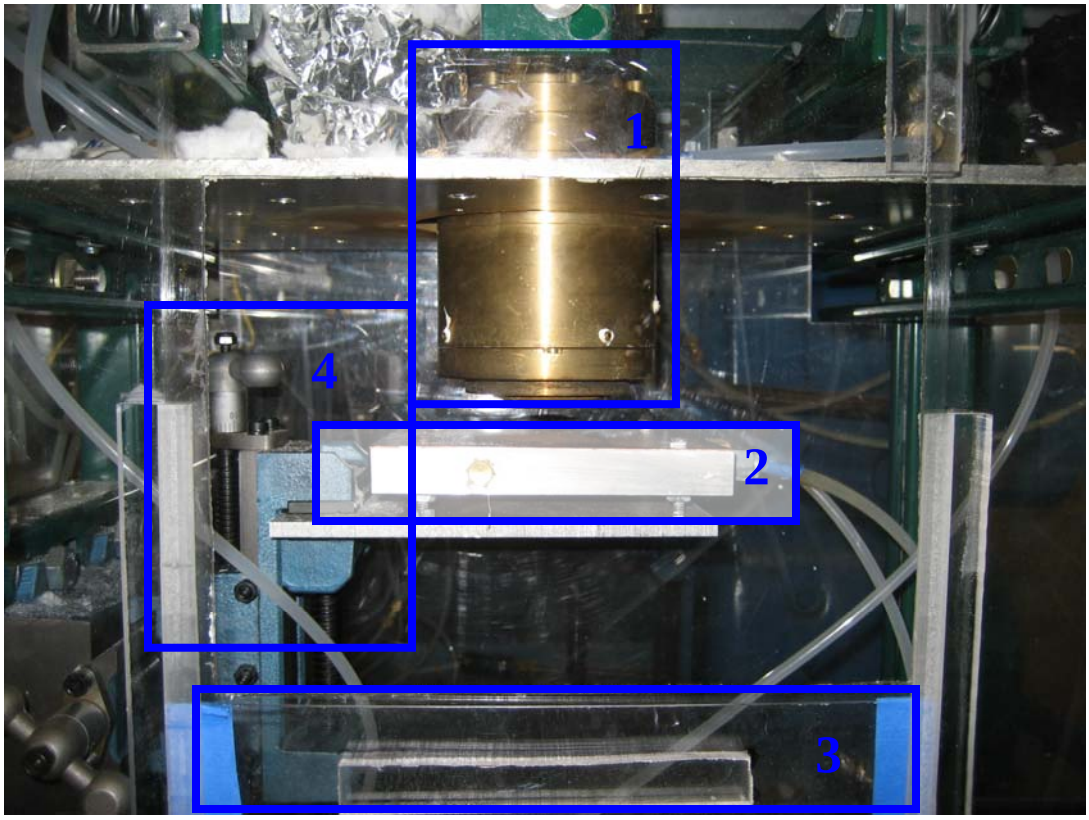

Figure 15 Experimental Setup. 1 – Burner, 2 – Substrate, 3 – Access door, 4 – Vertical position control

As can be clearly seen in Fig. 15, the whole setup is held together by UNISTRUT truss system, while all the elements of the system are encased by transparent acrylic. Another significant component of the setup is the two degree of freedom vice that holds the substrate. It allows adjusting vertical position of the substrate while running the

experiment, which allows observing the influence of the substrate location on the flame structure.

3.2 Line Setup

The gases primarily used in the experiment are CH_4, N_2, and compressed air. Several experiments were also performed with the addition of C_2H_2 and C_2H_4. Gas specifications are shown in Table 1.

Gas	Purity
Methane (CH_4)	CP Grade
Ethylene (C_2H_4)	CP Grade
Acetylene (C_2H_2)	CP Grade
Nitrogen (N_2)	High Purity

Table 1 Gas specification

Figure 16 shows the schematic of the gas system used in this experiment. Three gas tanks are connected to five MFCs that regulate the gas flow to the burner. Two flame arresters are installed on each line leg leading to the burner, while a third arrester is located before the split of the gas lines for increased safety.

The portion of the experimental setup that required the most time to implement was ferrocene addition system. The purpose of this system was to introduce vaporized ferrocene into the nitrogen flow, so that it could act as a catalyst for nanotube synthesis. Three different experimental precursor line configurations were attempted with only the last one yielding acceptable results. The main difference between setups was the location and the orientation of the ferrocene precursor feeder.

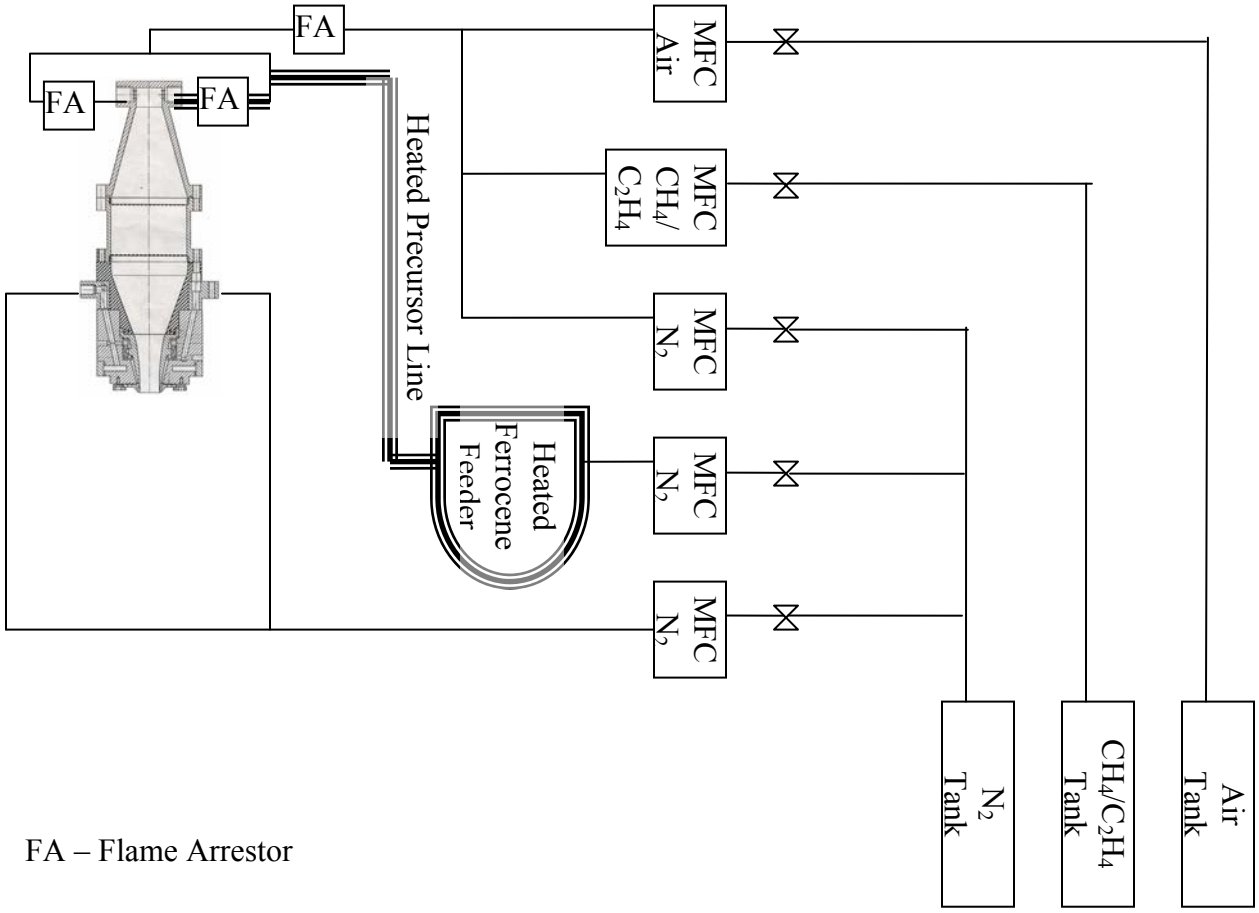

Figure 16 Experimental line layout

In the first attempted setup, the ferrocene precursor feeder was placed vertically outside of the main setup enclosure, due to the lack of space below the exhaust hood. In the second setup, the feeder was placed horizontally as to allow more ferrocene to be carried away by the precursor nitrogen.

Both setups proved to be extremely troublesome since ferrocene gases had to travel several feet before reaching the main line carrying fuel and oxidizer gases. As a

result, a long line heater had to be attached to the line to make sure that ferrocene vapor was not condensing inside of the line. Also, for every burner modification the precursor line and rope heater had to be taken out, which resulted in breakage of several rope heaters. In the second setup in particular, ferrocene clogging in the bends of the line became a common occurrence, which caused frequent replacement of the tubing as well as additional damage to the rope heater. Furthermore, the results obtained using such setup were unreliable, due to the fact that ferrocene would be delivered into the flame even when lines were clogged up. The ferrocene observed in the flame would come from ferrocene evaporation inside of clogged lines, which of course would not satisfy the desired loading rate.

The last setup is different from the two discussed above since the ferrocene feeder is only a few inches away from the main gas line leading to the burner. As a result, one small heater is used for heating both the feeder and the line after it. The gas line connecting the ferrocene feeder to the main gas line does not have any bends which ensures proper flow of ferrocene-carrying nitrogen.

Mass Flow Controllers (MFCs) are used to control the flow of the gases to the burner. The setup uses 5 MFCs, whose specifications appear in Table 2. The selection of MFCs was originally governed by the expected CH_4 laminar flame speed at rich equivalence ratios[56, 57]. Once the experiment was run several times, better suited MFCs were found to accommodate the necessary flowrates. For instance, it was found that MFCs do not function reliably when open to less than 2% of their capacity.

MFC	MODEL	FLOWRATE
Air	9701-A-95342/1	10 SLPM
Nitrogen	1802HC015730/10	2 SLPM
Nitrogen Precursor	9704HC035406/01	20 SCCM
Nitrogen Co-flow	101010168186003	10 SLPM
Methane/Ethylene	9803HC016580/06	2 SLPM

Table 2 MFC Specifications

The most consideration was given to picking a mass flow controller that governed the flow of nitrogen that carried ferrocene. The selection was governed by the required loading rate, which in turn was based on the Clausius-Clapeyron curve for the ferrocene. The chemical structure of ferrocene $Fe(C_5H_5)_2$ is shown in Fig. 17, with iron atom in the middle (shown in red), two carbon rings (shown in blue) with hydrogen (shown in yellow) attached to the carbon rings on the outside.

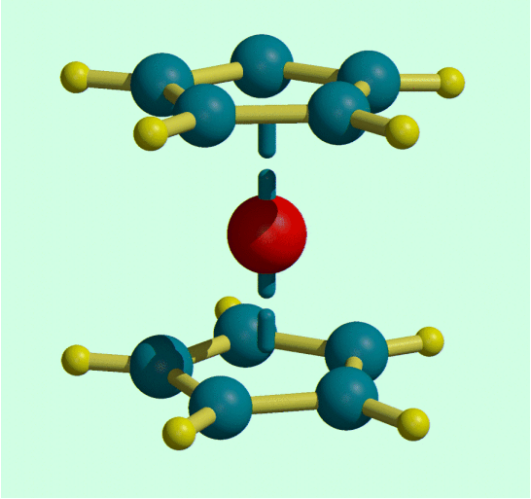

Figure 17 Ferrocene Structure

The precursor loading rate is given by

$$F_r = \frac{F_c P_r}{P_o - P_r},$$

where F_c is the flowrate of the carrier gas (L/min) at STP, P_o is the downstream pressure after the feeder (torr), and P_r is precursor thermodynamic vapor pressure at a certain temperature. P_r can be found through Clausius-Clapeyron relation, which for ideal gas simplifies to

$$P_r = P_1 \times \exp\left(\frac{H_{vap}}{R} \times \left(\frac{1}{T_1} - \frac{1}{T_r}\right)\right),$$

where P_1 is atmospheric pressure, R is universal gas constant equal to 8.314 kJ/kmol *K, T_1 is ambient temperature, T_r is ferrocene temperature and H_{vap} is enthalpy of vaporization that is equal to 74 kJ/kmol for ferrocene, based on experimentally obtained and theoretical values[58].

Based on the work done by Vander Wal and Hall[46], ferrocene loading rate was chosen in the range between 1 and 50 mg/min. The first set of experiments used a loading rate of 22 mg/min, which corresponded to 0.05 SLMP flow of N_2, when the ferrocene feeder was at 180° C. However, as need for lower loading rate became transparent, due to insufficiently small catalyst particles, a much lower loading rate was utilized by employing a 20 SCCM mass flow controller.

Ferrocene itself was chosen based on the fact that many researchers have used it as a catalyst precursor for CNT synthesis. Some of the criteria that made it especially attractive are low vaporization temperature and product hazard considerations.

The software used to control MFCs is Labview. The typical Labview interface is shown in Fig. 18. To find the appropriate percentage for the MFC to be open corresponding to the desired flowrate, K factor for each gas had to be taken into the account. K factors used are illustrated in Table 3.

Gas	K factor
Methane	0.725
Acetylene	0.58
Ethylene	0.6
Nitrogen	1.011
Oxygen	1.003

Table 3 K Factors used in calculating mass flowrates

Based on K factors, total experimental volumetric flowrate is found by dividing theoretical flowrate by K factor. Then, the percentage that the MFC needs to be open is found by dividing experimental volumetric flowrate by the total volumetric capacity of the MFC.

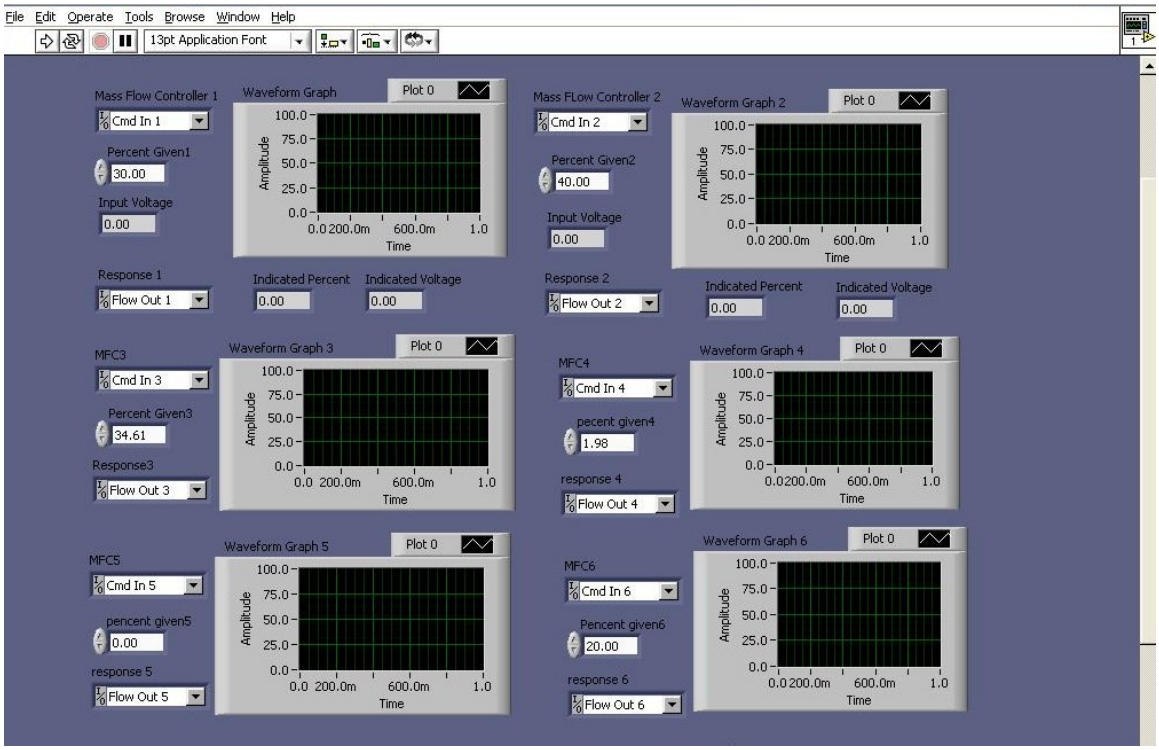

Figure 18 Labview interface

3.3 Velocity and Temperature Selection

Velocity and temperature play critical role in the flame structure as well as the synthesis of carbon nanotubes. Early runs with the experimental setup showed that the stagnation premixed flame is extremely sensitive to even minute disturbances, which cause the flame either to flashback or blow off. Velocity for the experimental conditions was chosen based on the methane laminar flame speed, which peaks at about 40 cm/sec for the equivalence ratio equal to one, but goes down to 25 cm/sec at 1.3 equivalence ratio[59]. Most of the results were obtained at 1.2 equivalence ratio, where the laminar flame speed is between 27 to 28 cm/sec, depending on N_2 dilution.

The temperature was mainly controlled by N_2 addition. As N_2 was added, temperature of the flame went down. The correlation of N_2 dilution to temperature was obtained from literature[56], as well as from adiabatic flame temperature calculations performed using STANJAN.

3.4 Experimental Procedures

3.4.1 Synthesizing CNTs

1) Turn on roof fan.
2) Turn on tap water for burner cooling and adjust needle valve as needed.
3) Turn on substrate cooler.
4) Open house air.
5) Open nitrogen and then methane/ethylene tanks.
6) Open mass flow controllers.

7) Enter percentage open for all mass flow controllers in Labview and run the program.
8) Ignite the flame with the auto-igniter.
9) Once flame is established, turn on the temperature controller.
10) Raise the temperature of the ferrocene feeder to the desired temperature (150-215° C) depending on the desired size of the precursor particles.
11) Once feeder reaches desired temperature, place tungsten wire on the substrate just below the flame.
12) Make sure that ferrocene deposits on the surface of the substrate and the tungsten wire. Presence of ferrocene should be manifested by the orange powder layer. If no such layer is present it can potentially mean:
    a) Feeder temperature is too low and ferrocene particles depositing on the substrate are so fine as to seem invisible to the naked eye.
    b) Ferrocene precursor line is clogged up and needs to be cleaned.
    c) There is not enough ferrocene in the feeder.
13) When running the experiment, make sure there is no condensation on the substrate. At the same time make sure it is not too hot, which can potentially damage the burner. Regulate the flow of cooling water using a needle valve.
14) Once the experiment is completed proceed to shutdown:
    a) Lower the feeder temperature to 20° C.
    b) Redirect cooling water from the tap from substrate to the feeder using the three way valve.

c) Once the feeder temperature drops below 100° C turn off the methane/ethylene mass flow controller.

d) Turn off nitrogen mass flow controller once methane/ethylene pressure drops below 5 psig.

15) Once flame is extinguished close all mass flow controllers and verify that all gas tanks are closed.

16) Turn cooling water to the burner and feeder off.

17) Turn off Labview

18) Turn off compressed air.

19) Turn off roof fan.

3.4.2 Ferrocene Feeder Refill Procedure

1) Take off all the insulation from the feeder and precursor lines.
2) Disconnect the feeder from the precursor lines.
3) Disconnect feeder cooling system.
4) Disconnect thermocouple cable from thermocouple.
5) Place the feeder upside down in a vice and secure it.
6) Put ferrocene in the feeder.
7) Remove old Teflon tape of the threads of all connectors, and re-apply new Teflon.
8) Attach feeder to the precursor line, making sure that connections are tight and there are no leaks.
9) Re-connect feeder cooling system.
10) Re-connect thermocouple to thermocouple cable.
11) Place insulation over feeder and precursor lines.

3.4.3 TEM Sample Preparation Procedure

1) Cut tungsten wire in 1 to 1.5 cm long pieces.
2) Ultrasonicate tungsten wire in ethanol for 5 minutes.
3) Collect samples on the tungsten wire.
4) Ultrasonicate samples in ethanol for 5 minutes.
5) Place TEM grid onto weighing paper with appropriate tweezers.
6) Put a drop of the solution on the TEM grid.
7) Allow solution to dry.
8) Place TEM grid into the grid holder. When using copper TEM grid make sure to place solution onto copper side.

3.5 Characterization Techniques

The analysis of the experimental results is performed using Field Emission Scanning Electron Microscope (FESEM), Transmission Electron Microscope (TEM), Electron Dispersion Spectroscopy (EDS), and Raman Spectroscopy.

FESEM with EDS is used for the analysis is Zeiss Gemini 982 located in the Materials Science and Engineering Department at Rutgers University. The information on elemental composition of samples is obtained with FESEM EDS, which is critical in establishing the optimal configuration of the ferrocene line.

TEM analysis is performed on a LEO/Zeiss 910 TEM at Princeton University PRISM facility. This TEM operates at 100 KeV and is equipped with a CCD camera that allows taking and viewing digital images in real time. TEM is the most useful tool in

revealing the presence and size of precursor particles. MWNTs and nanofibers are observed using TEM as well.

Raman spectroscopy using 532 nm excitation wavelength is utilized to detect the presence of SWNTs as well as MWNTs. The Radial Breathing Mode (RBM) of the Raman spectrum, located between 75 and 300 cm^{-1}, allows identification of the presence of SWNTs, and calculation of their diameter[60]. The D-band of the spectrum on the other hand served as an indication of MWNTs and amorphous carbon presence in the sample[61], while the G-band serves as another indication of SWNTs presence[62]. The theoretical range of CNT signal is 1500 to 1605 cm^{-1} for the G-band and 1250 to 1450 cm^{-1} for the D-band, depending on the excitation frequency used[62].

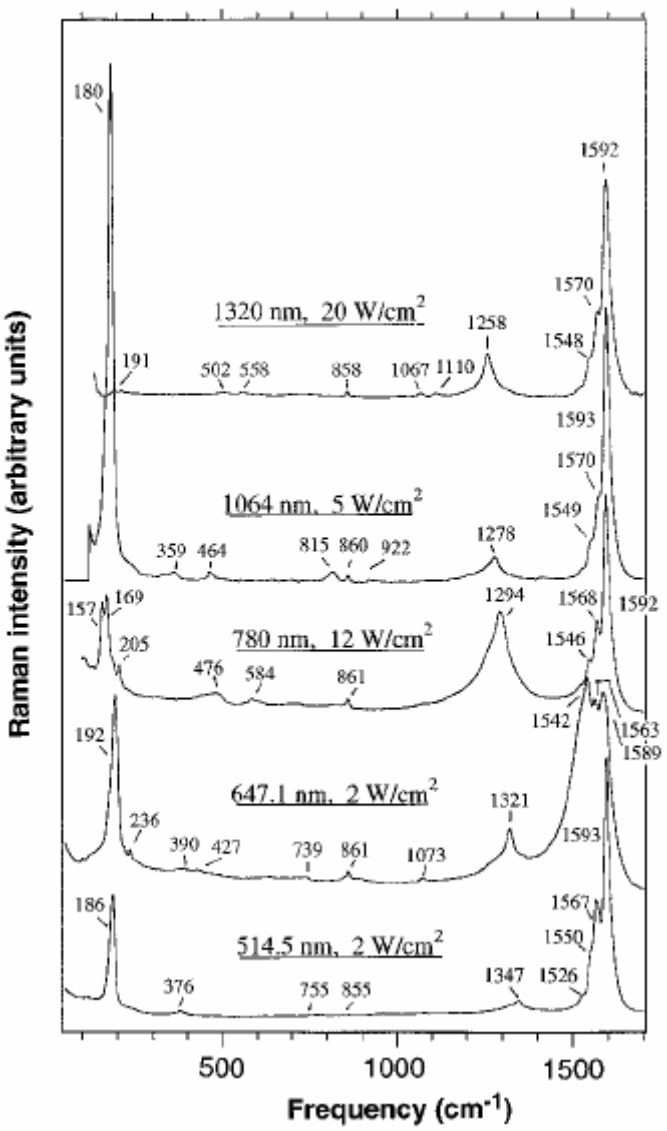

Figure 19 Variance in Raman spectra of SWNTs depending on laser excitation frequency[63]

The choice of excitation wavelength for determining the presence of CNTs is important but not critical. As *Rao et al*[63] shows, excitation wavelengths from 514.5 to 1320 nm can be used to obtain the spectra that do not differ significantly. For instance, the RBM obtained using 534.5 nm excitation wavelength is at 186 cm^{-1}, while using 647.1 nm excitation wavelength results in RBM at 192 cm^{-1}. Figure 19 shows Raman CNT peak dependence on the excitation wavelength used.

Bandow *et al*[64] postulated the correlation between the observed RMB frequency and the size of the nanotube, while implicitly stating that RBM is only a function of the nanotube diameter but not its helicity. The relationship states:

$W_r = 223.75(cm^{-1}nm)/d(nm)$,

where d is the nanotube diameter and W_r is the RBM frequency.

3.6 Numerical Techniques

The flame simulation is accomplished using a numerical mechanism that estimates the reactions occurring in the quasi one-dimensional stagnation point flame. The structure of the mechanism is shown in Fig. 20:

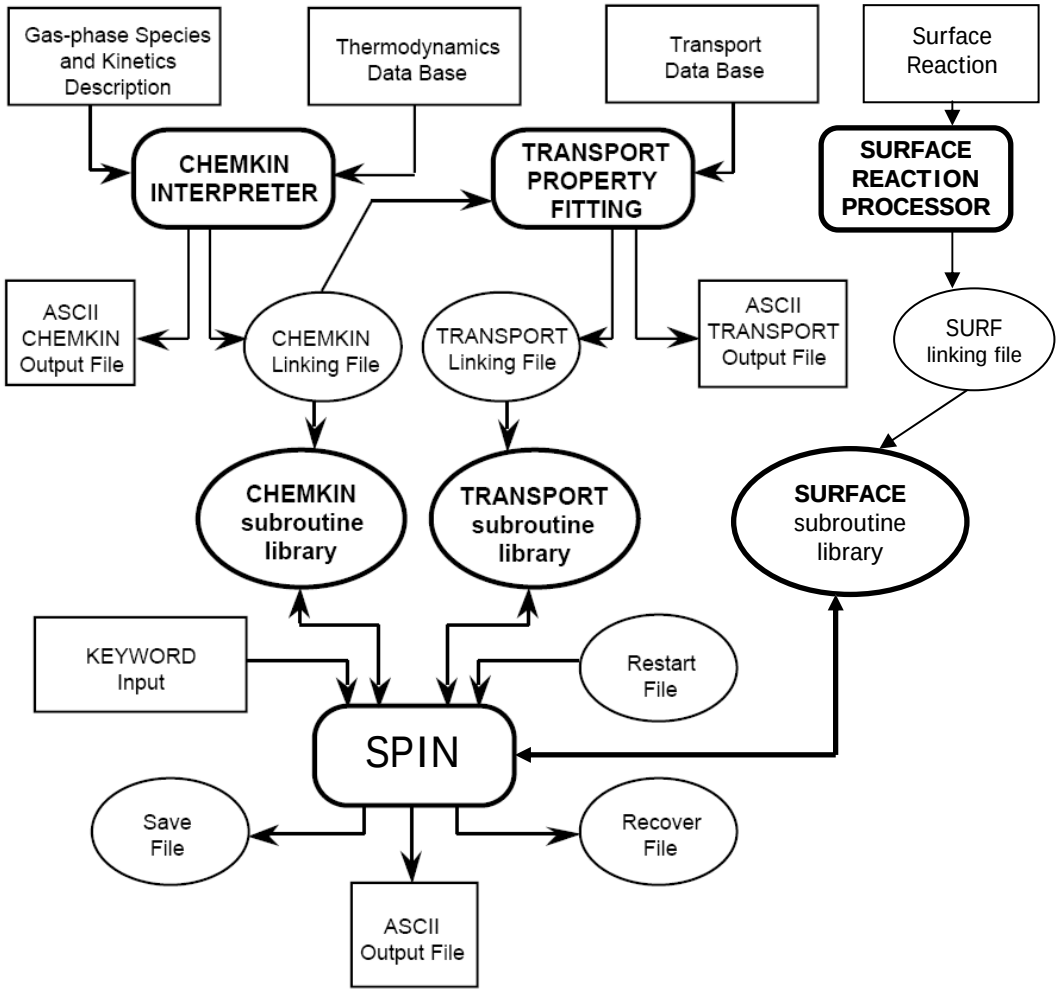

Figure 20 Numerical simulation mechanism used in this study

Chemkin Interpreter, Transport Property Fitting and Surface Reaction Processor are three basic mechanisms that work together to simulate basic chemical reactions in the one-dimensional flat flame. Chemkin Interpreter acquires species and thermodynamics information to generate the chemkin linking file. Transport Property Fitting uses transport database to create transport linking file. Surface Reaction Processor uses a

surface reaction input to create a surf linking file. SPIN uses previously created subroutine libraries and the user modified SPIN input file to generate output file.

The procedure for typical execution of the code from start to finish is as follows:

1) make –f Makefile_0
2) ./chem.exe<chem.inp
3) make –f Makefile_1
4) ./surf.exe<surf.inp
5) make –f Makefile_2
6) ./tran.exe
7) make –f Makefile_3

Perform these steps only if mechanism code is modified

8) vi input_file_name.inp
9) ./spin.exe<input_file_name.inp>spin.out
10) cp save.bin rest.bin

The first 7 steps are only necessary if the core mechanisms are changed. Otherwise, if mechanisms remain the same only steps eight through ten are necessary. Several other additional FORTRAN programs, such as addition or removal of grid points, can be employed to modify the restart files and make the SPIN processor run more efficiently.

The input file allows specifying several critical parameters that define the flame, as well as the assumptions that allow the simulation to find a solution. The most important parameters specified are flame velocity and gas composition. The boundary conditions are specified through setting the temperatures at the burner exit and at the substrate.

The solution can be obtained in two ways. First, if no previous solution is available and thus no restart file exists, an initial temperature profile needs to be estimated. The

simulation is run, and based on the results, the estimate is modified until the simulation runs successfully yielding the desired solution. Alternatively, the simulation can run based on the restart file that is obtained from previous runs.

SPIN was successfully used by Hinkov *et al*[65] to simulate the dependence of SWNT formation mechanism on pressure. The mechanism allowed understanding the variation of radical presence in the flame with pressure and temperature.

Chapter 4. Results and Discussion

4.1 Flame Structure

While the experiments are performed using various equivalence ratios, flame speeds and other characteristics, the flame structure is always taken into the account. The flame has to be located between the burner nozzle and the substrate in a way that the flame would not be too close to the substrate, but also not flashing back into the burner.

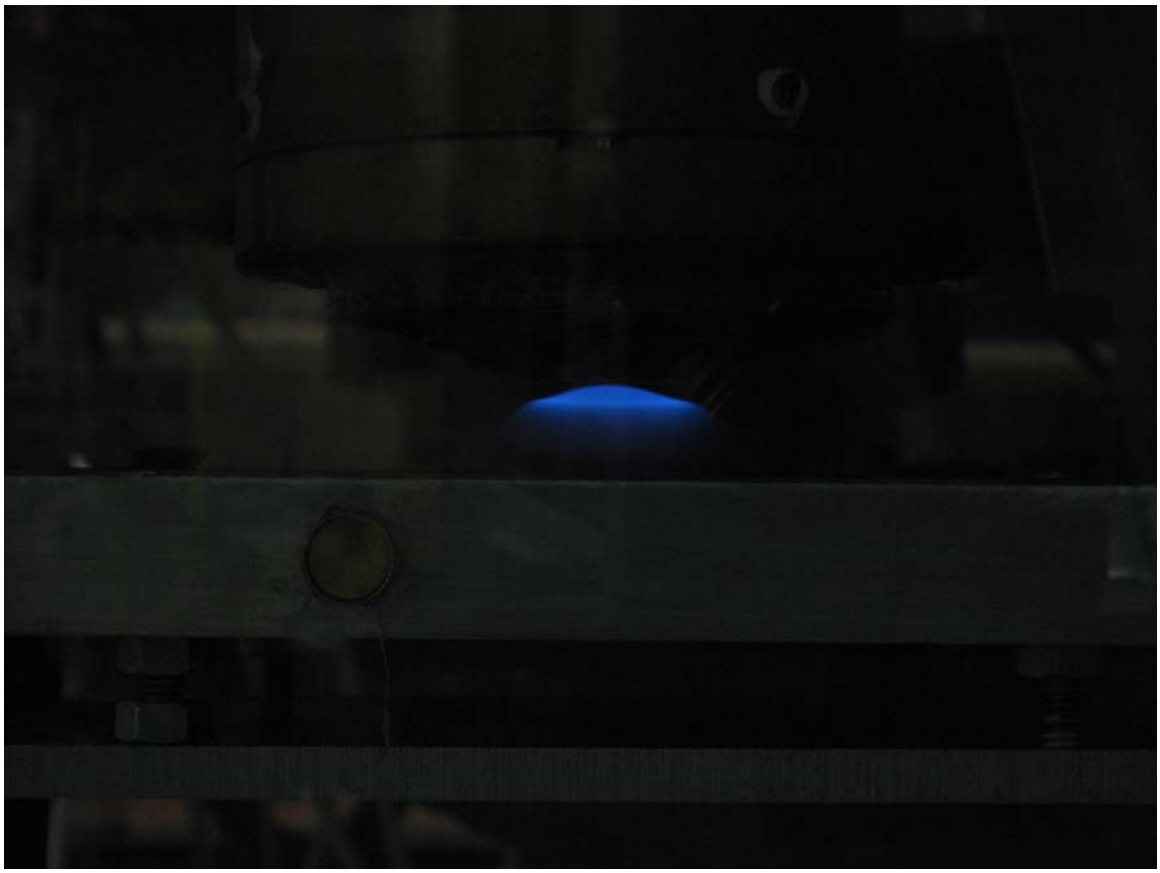

Figure 21 A typical flame at 1.2 equivalence ratio and gas velocity equal to 27.5 cm/sec

As Fig. 21 shows, the flame is not perfectly flat before ferrocene is added. That could be easily corrected by diluting the flame with excess nitrogen. That in turn would

lower the temperature of the flame, which is not desirable for this particular experimental condition.

The reason why the flame cannot be located close to the substrate is the risk that CNTs would form via substrate formation route on the substrate itself if its temperature is too high. Being that the object of this study is gas-phase CNT formation, substrate growth needs to be avoided. An additional benefit of having a flame further from the substrate is to allow for more residence time for CNTs to grow after they are formed in the flame. Finally, as the flame approaches the substrate, the co-flow nitrogen becomes less and less effective in stopping outside air from entraining into the flame, changing reaction and flame characteristics.

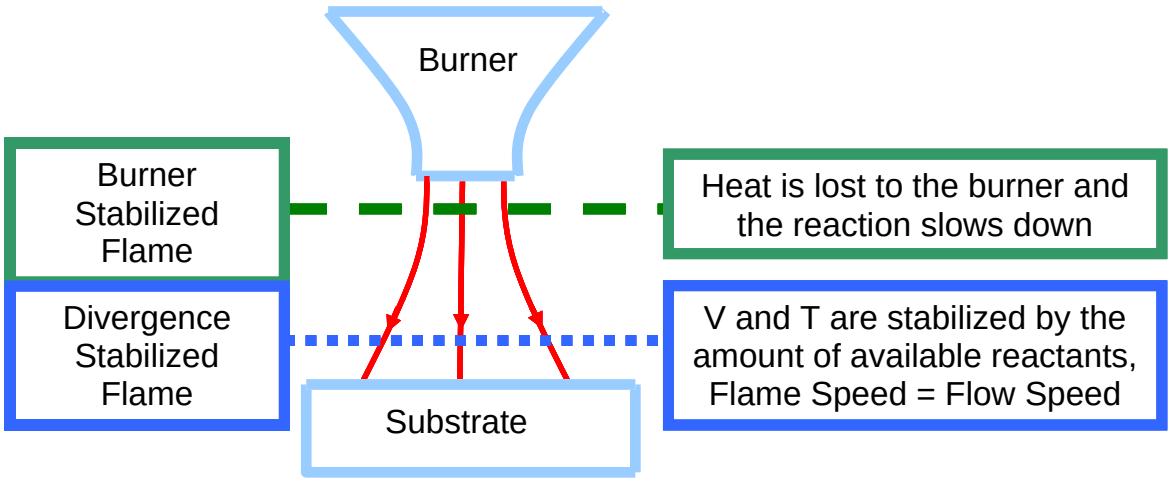

Figure 22 Two modes of flame stabilization

As Fig. 22 shows, the location of the flame is critical and governs the stabilization regime of the flame. If the flame is very close to the burner, then the flame's energy will be lost to the cooled surface of the burner due to quenching and the flame will have difficulty shifting from its location even if the equivalence ratio is changed or the gas

velocity is increased. However, when the shift does occur, the flame can shift near to the substrate or be completely extinguished due to the perturbations associated with a rapid flame regime change.

Another more favorable alternative stabilization regime is divergence stabilization. Velocity and temperature are both governed by the presence of reactants necessary for the reaction to take place. This regime insures that the laminar flame speed is equal to the gas flow speed.

We employ a divergence stabilization regime in the discussed experiments, even though the flame is very close to the burner. The observed gas flow velocity matches theoretical laminar flow speed, which would not be the case if the flame is burner stabilized.

The biggest influence on the flame position, however, is by far exerted by ferrocene addition. In fact, as it is shown in this experiment and observed by Tian *et al*[N66] that ferrocene quenches the flame by reducing the laminar flame speed. The impact on the flame structure can be seen in Fig. 23. Comparing to Fig. 21 where no ferrocene is added, it is clear that the flame shifts down and becomes almost completely one-dimensional, instead of curved as before. Ferrocene addition is clear as well, since the orange color underneath the flame can be attributed to ferrocene particles.

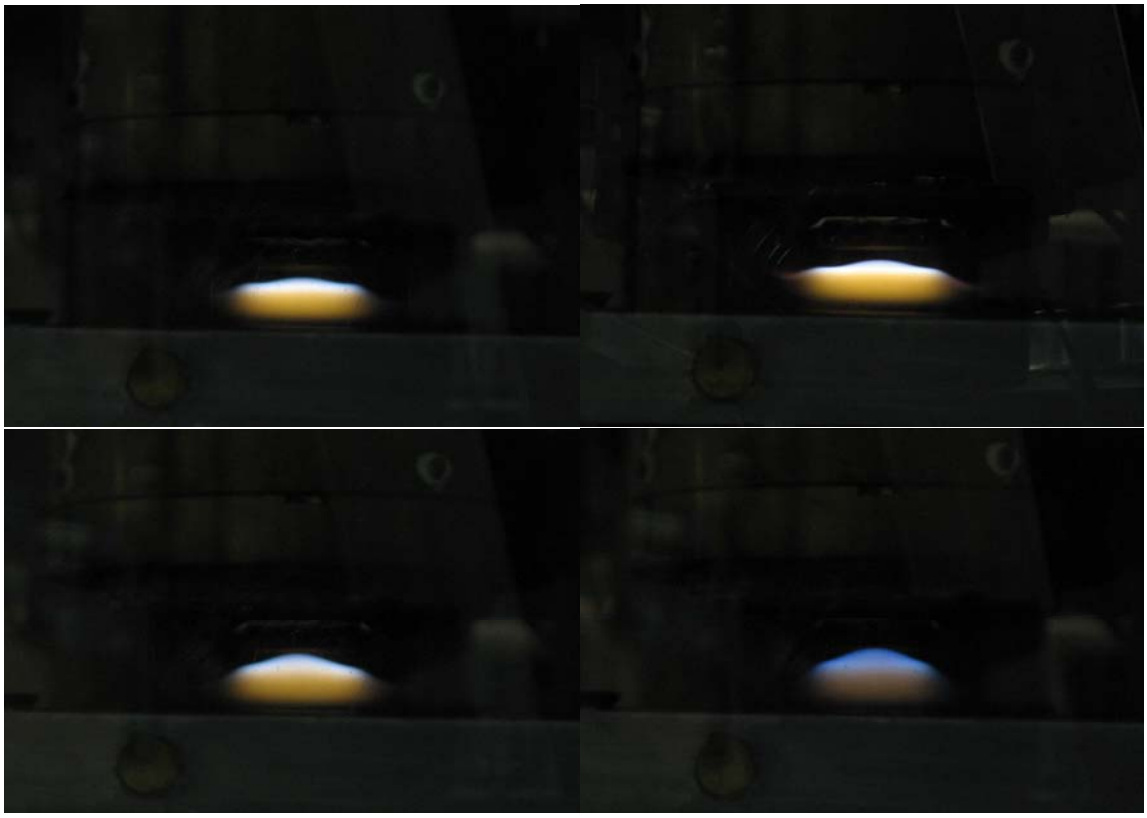

Figure 23 Influence of ferrocene addition on flame structure. A – ferrocene feeder at 75° C, B – ferrocene feeder at 120° C, C – ferrocene feeder at 150° C, D – ferrocene feeder at 165° C

The glow becomes more apparent when the temperature of the ferrocene feeder goes from 75 to 120° C, but decreases as the temperature increases until it reaches 165° C. The shape of the flame also reverts back to being more curved. The reason for this trend is that at first there is no ferrocene particles added to the flame. Once the temperature of the feeder goes up, there is more and more ferrocene entering the flame. However, the particle size goes up with feeder temperate as well. As the size of ferrocene particles increases, they are not able to quench the flame as effectively as smaller particles, due to the decreasing surface area. Similarly, they do not emit as much of an orange glow as their smaller counterparts.

It should be noted that all the pictures seen above are taken with the acrylic gate blocking the flame. Lowering the gate even for a few seconds necessary for taking the picture disturbs the flame and results in a flame flashback, as shown in Fig. 24.

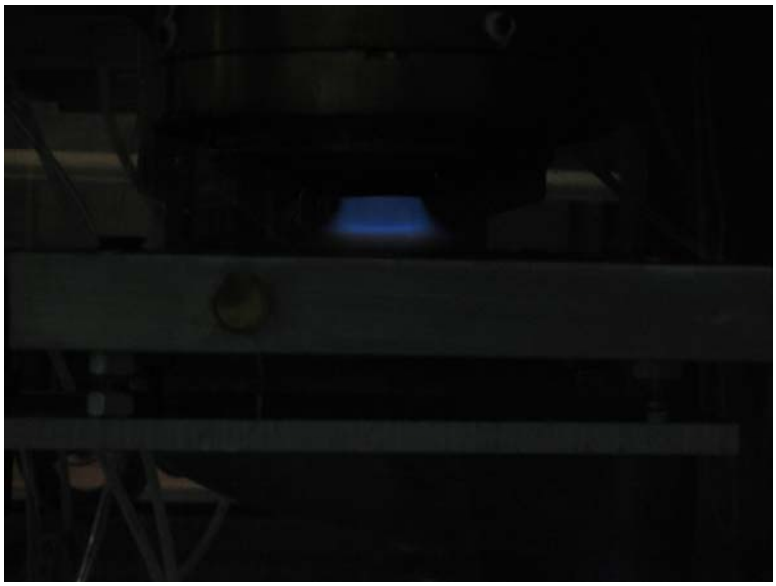

Figure 24 - Picture of a flame taken with lowered acrylic gate

The Clausius – Clapeyron relation discussed earlier allows one to graph the loading rate. As Fig. 25 shows, the loading rate until approximately 120° C is minute, especially compared to the loading rate at 165° C. Thus, it is reasonable to conclude that the orange glow present in the region below the flame emanates from ferrocene that is not vaporized, but is rather in the solid form. This also agrees with the previous observation of decreasing glow with the increasing feeder temperature.

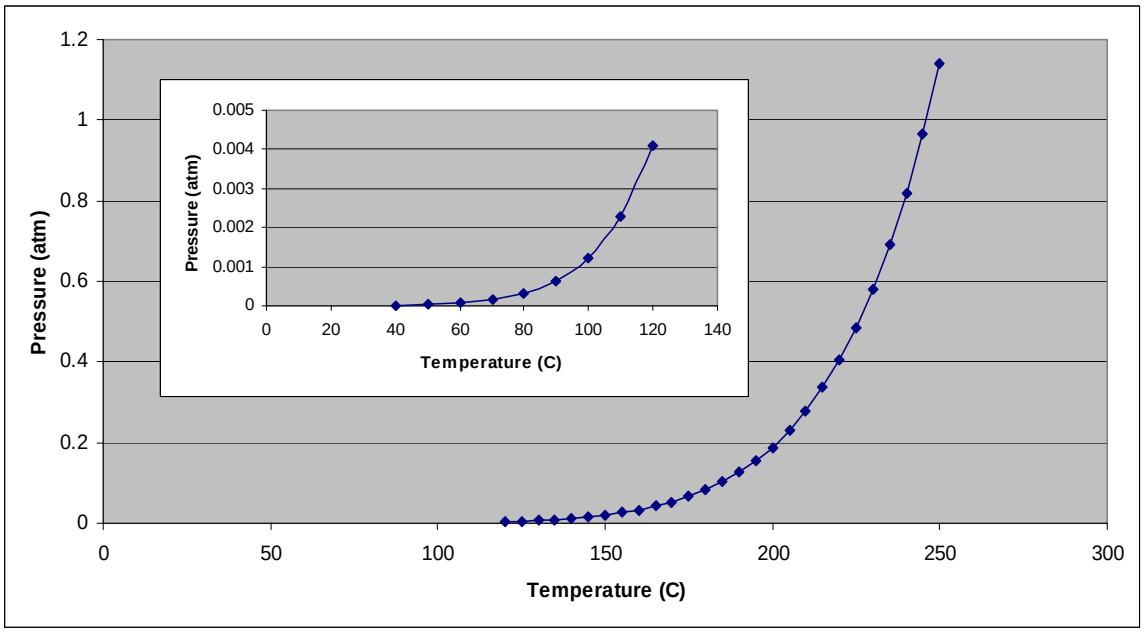

Figure 25 Ferrocene loading rate dependance on feeder temperature

4.2 Nanofibers

The first significant set of structures observed using FESEM and TEM are nanofibers. These structures are obtained at equivalence ratio equal to 1.2. The diameter of a nanofiber in Fig. 26a is approximately 50 nm, while the diameter of nanofiber in Figure 26b-c is 25 nm.

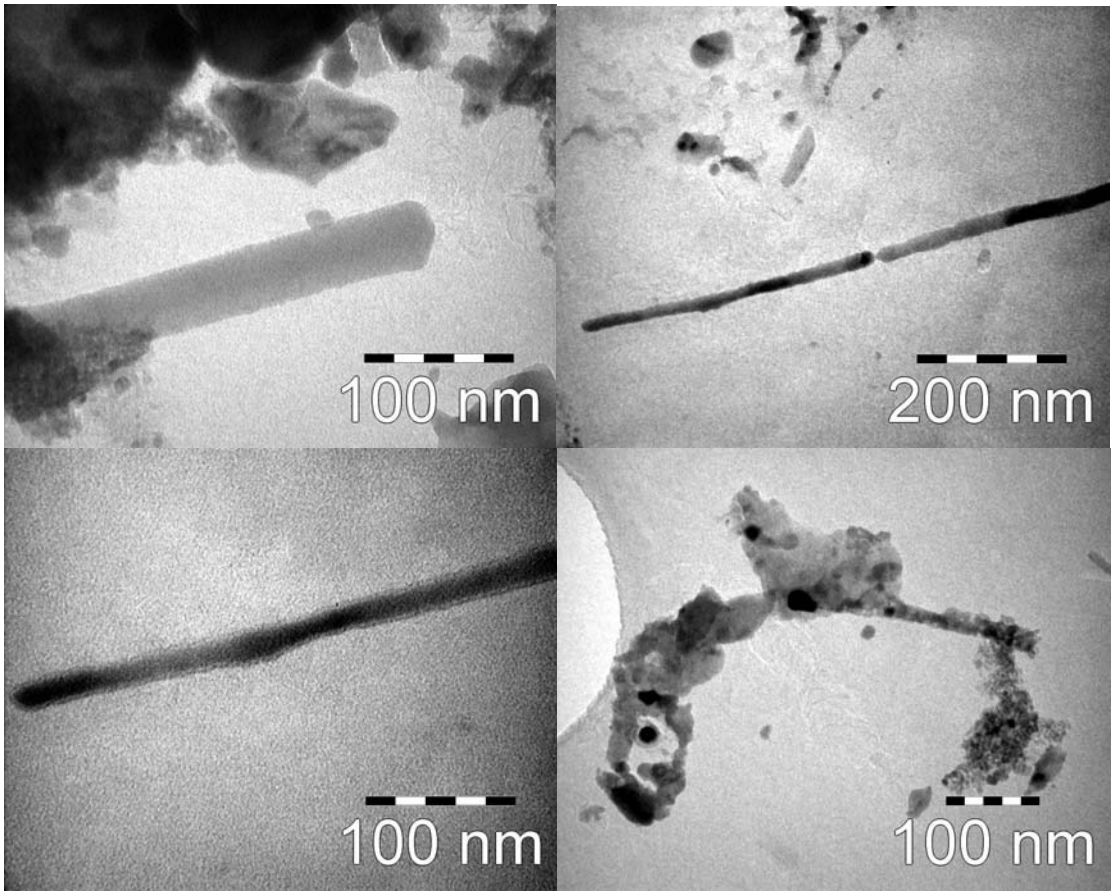

Figure 26 A - nanofibers generated using 1.2 equivalence ratio. B, C – the same nanofiber at different magnifications at 1.2 equivalence ratio. D – nanofiber encased by amorphous carbon

Based on the images above, one can argue that nanofiber growth initiates from the particle appearing darker than the rest of the fiber and located at the end of the rod, clearly seen in Fig. 26b-c. However, it can also be noticed that darker regions do not

form a circular spot that would be characteristic of the round catalyst, but rather a whole region up to 40 nm in length that appears darker than the rest of the nanofiber.

Obtained images also illustrate a common problem that re-occurs throughout experimental runs at most of the settings, which is the abundance of amorphous carbon that often conceals other structures. Figure 26d shows a possible nanofiber that is almost invisible behind the layer of the amorphous carbon. Also, it is interesting to observe that catalyst particles are not uniform in diameter, even though the experiment is run under constant settings. It is possible that the flow of nitrogen that carries catalytic ferrocene from the feeder to the burner is too high. As a result, flow is not only picking up small vaporized ferrocene particles, but possibly much larger particles that are not fully vaporized. Another possible explanation could be that larger particles seen on the image does not come directly from the feeder, but are rather accumulated at the burner exit or in the mixing chamber during previous runs.

The later explanation seems very likely, especially since systematic cleaning of the burner shows ferrocene accumulation inside of the burner. The reason for ferrocene to settle on the burner walls is the same reason why nanotubes would settle on the tungsten wire once they are generated in the flame. Thermophoretic effect between vaporized ferrocene at temperature above 150° C and water-cooled burner at 20 to 30° C ensures that some ferrocene would inevitably coat the burner. As previously discussed, this drawback cannot be readily corrected, since the burner needs to be maintained cool so that internal components do not melt, as well as to prevent flashback.

To better understand the critical factor behind the formation of nanofibers, the experiments are also conducted at equivalence ratios equal to 1.3 and 1.4. It is generally

believed[32] that nanotubes form at the equivalence ratios just below the equivalence ratio window where soot begins to form, so nanostructure formations are expected at higher equivalence ratios.

However, as Fig. 27 shows, carbon nanofibers are not present at those equivalence ratios. One reason could be that observed particle size 3-5 nm is on the lower allowable range for nanofiber formation.

The circled regions are interesting because they show particles connected in a bead-like elongated pattern. Resolution of 100 KeV TEM does not allow for positive establishment of the nature of these structures, but SWNTs and MWNTs are often found connecting catalyst particles. However, resolution of 5 to 10 nm is needed to make such determination.

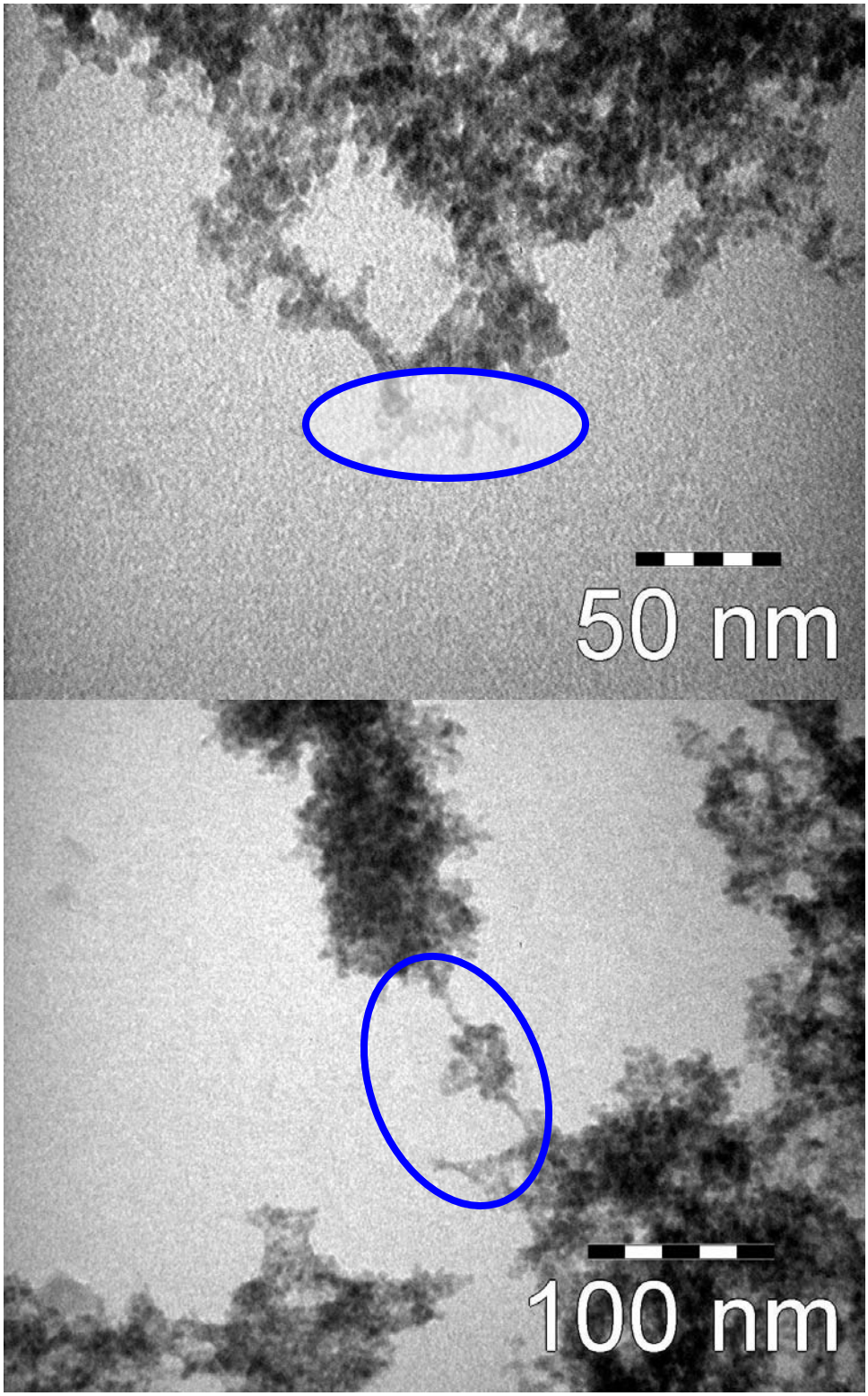

Figure 27 A – sample image taken at 1.3 equivalence ratio. B – sample image taken at 1.4 equivalence ratio

Now that the precursor variance in observed nanofibers images has been mentioned, it is time to discuss its importance. Similar to the growth of nanotubes, the growth of nanofibers proceeds upon carbon atoms attaching themselves to the catalyst. Rodriguez[19] in fact believes that nanofiber growth follows the Baker growth model discussed earlier. The key difference is that instead of the hollow tube being formed by the arriving carbon atoms, it is a carbon sheet. The critical factor determining if the structure formed is nanofiber or nanotube is the catalyst particle size. In fact, Rodriguez[19] observed that nanofibers only form if the catalyst is larger than 3.5 nm.

Images showing fibers are also obtained using FESEM. Equivalence ratio is varied from 1 to 1.4, while the feeder temperature is set at 175° C. It is expected that catalyst particle size at this temperature would be much bigger than that necessary for CNT formation, but perfect for nanofiber formation.

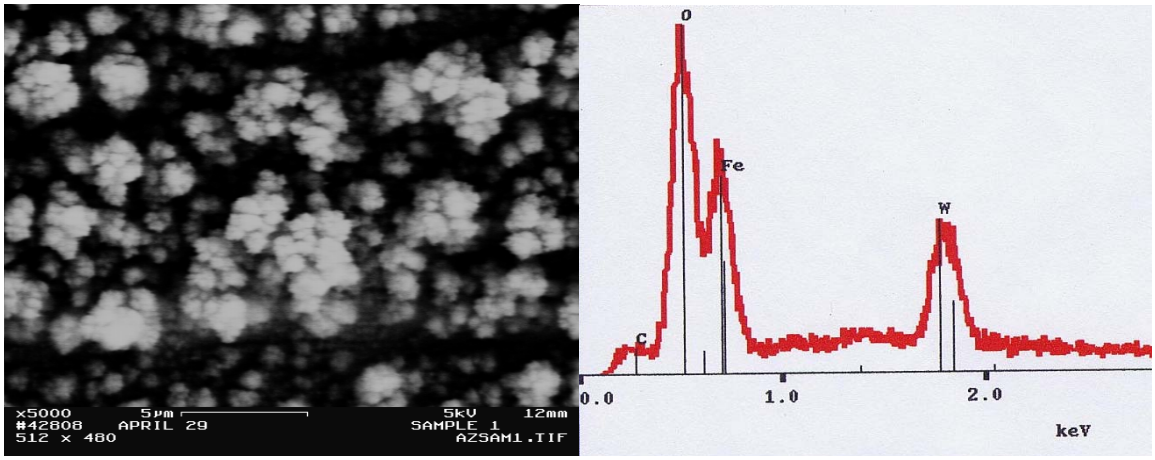

Figure 28 FESEM and EDS images of the samples obtained at 1.0 equivalence ratio

From Fig. 28 it is clear that no fibers were formed using this experimental condition. Although EDS shows a very small peak for carbon as well as a large peak for the

ferrocene, which indicates an adequate supply of iron atoms, it seems that most observed structures are iron oxide, clustered in spherical shapes that range from hundreds to thousands of nanometers in diameter.

At 1.1 equivalence ratio the picture changes, as seen in Fig. 29. Although EDS shows exactly same elemental peaks as at stoichiometric ratio, FESEM shows the decrease of iron oxide concentration. Instead, it is carbon nanofibers several hundred nanometers in diameter that start to appear.

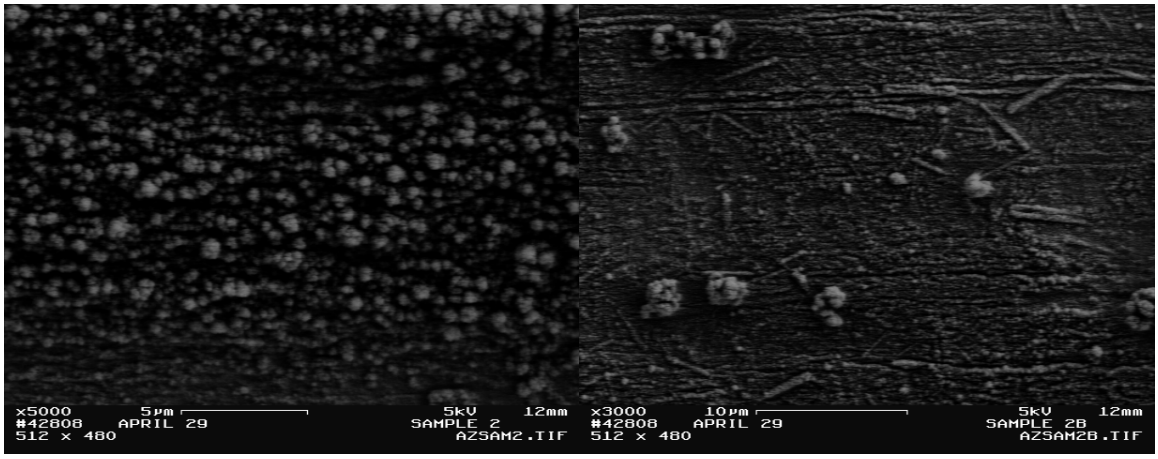

Figure 29 Nanostructures observed at 1.1 equivalence ratio

Some factors that can account for the variation in images observed above are possible hot spots on the tungsten wire. Although the wire is in direct contact with water-cooled plate, the contact point is small, which obviously limits heat dissipation to the substrate. Thus, the points of tungsten wire that have better contact with the substrate are cooler and could facilitate completely different nanomaterial growth than those regions that are at a higher temperature.

As we move to 1.2 equivalence ratio, a multitude of fibers shown in Fig. 30 is observed.

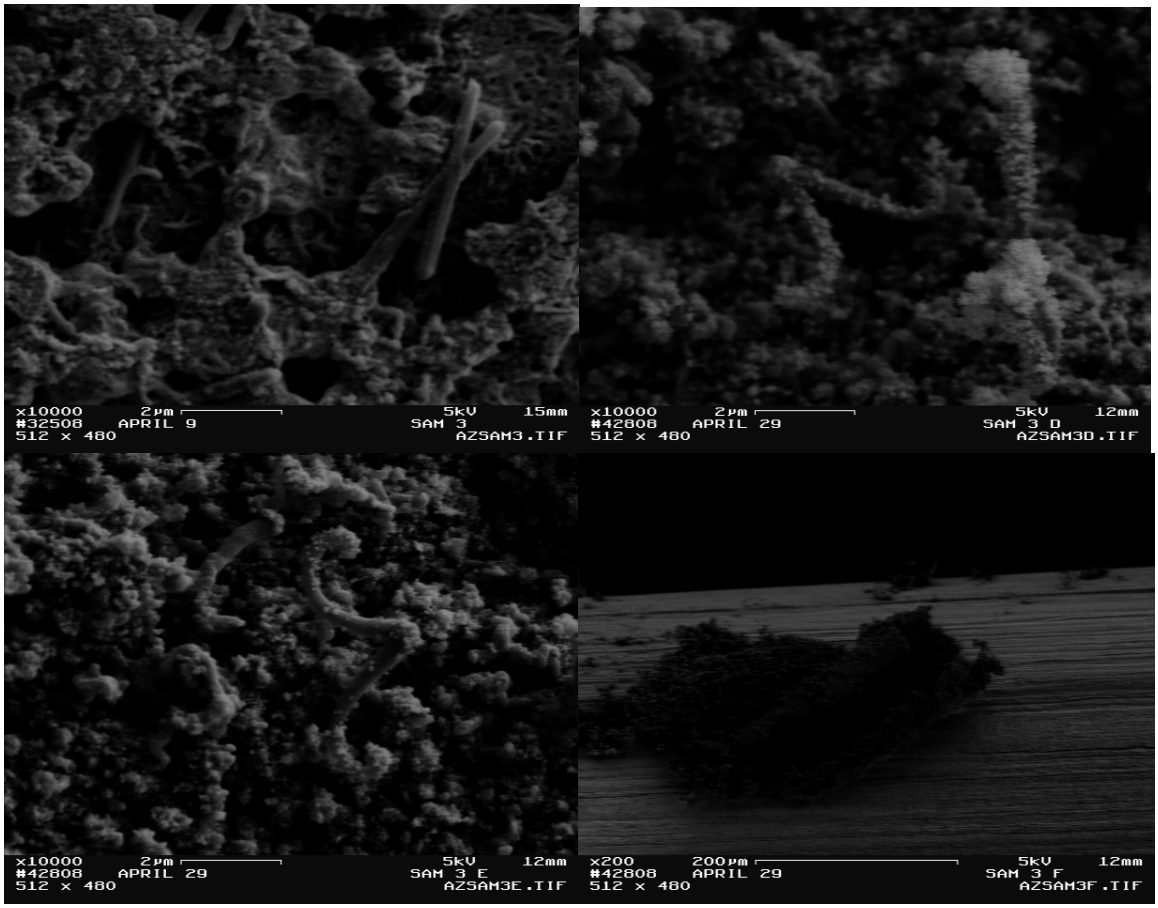

Figure 30 Fibers observed at 1.2 equivalence ratio

As before, the structures are several hundred nanometers in diameter, but now straight as well as helical fibers are observed, all reaching 5 to 7 micrometers in length. Interestingly, the structures shown in Fig. 30a-c all form in the sooty region depicted on Fig. 30d. The sooty patch is very significant in size and can be observed with the naked eye on the tungsten wire. What is not clear however is if the patch formed in the flame via aerosol method, or grew on the substrate due to a hot spot that allowed for sufficiently high temperature necessary for nanostructure growth. However, based on the random positioning of the fibers that do not show a preferred orientation, it seems likely that these structures precipitated from the flame.

The EDS of areas shown in Fig. 30 demonstrates evidence of carbon based structures, as peak for carbon exceeds all the other peaks in strength, while the oxide peak subsides from its previous level to the level of ferrocene concentration. The EDS image is shown in Fig. 31.

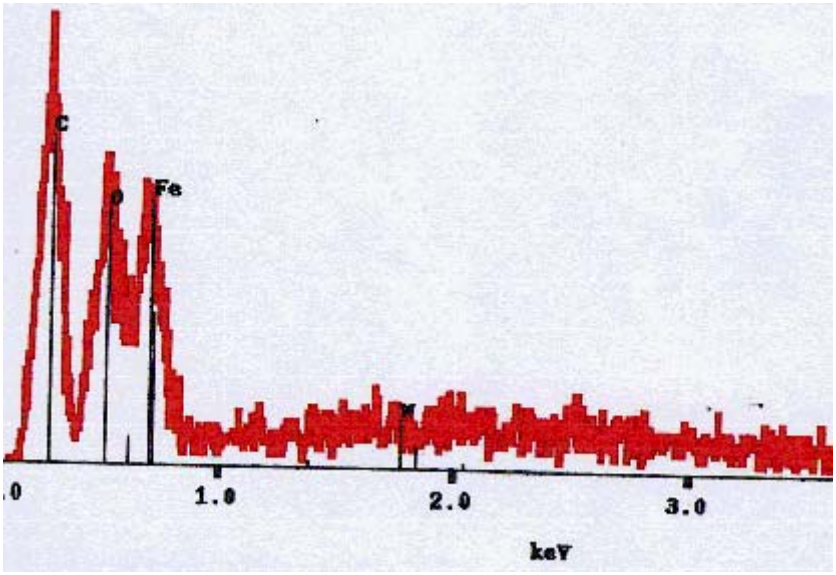

Figure 31 EDS image showing chemical composition of samples obtained at 1.2 equivalence ratio

The images demonstrated in Fig. 32 and obtained using equivalence ratio of 1.3 show resemblance to the samples generated using 1.1 equivalence ratio. As in that case, there are some spheres that EDS confirms as being iron oxide. However, the fibers are still present in the regions covered with soot, even though not in the amounts found at 1.2 equivalence ratio.

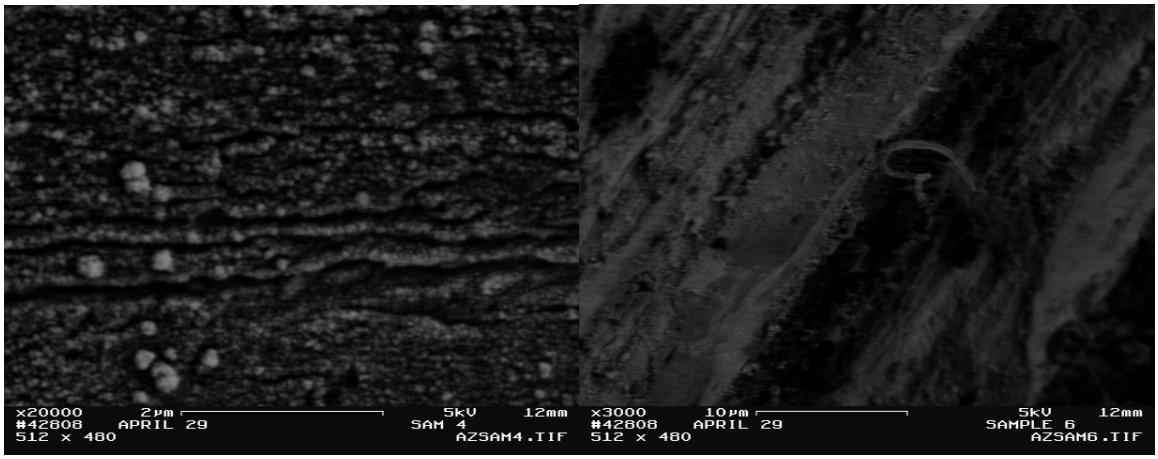

Figure 32 Images obtained at 1.3 equivalence ratio

Finally, at equivalence ratio equal to 1.4 no significant nanostructures are observed. The above observations show a clear trend in fiber formation. The optimal equivalence ratio is 1.2, while some nanotubes can be observed at other equivalence ratios close to 1.2.

4.3 MWNTs

Multi-wall nanotubes are generated in this experiment using ethylene as a fuel. In fact, most researchers have used ethylene in the past with only a handful using methane.

Using equivalence ratio of 1.27 and gas velocity of about 27 cm/sec MWNTs are synthesized in the flame. Similar to MWNTs depicted on images obtained by Wander Val and Ticich[50], Merchan – Merchan *et al*[40] and Murr *et al*[51], which are discussed as part of literature review, these MWNTs are coated with amorphous carbon, as seen in Fig. 33. The diameter of the nanotubes are about 5-7 nm, with lengths approaching 100 nm. It is clear that nanotubes are not arranged in an organized pattern, which is to be expected being that material deposited on the tungsten wire is ultrasonicated before being placed on the TEM grid.

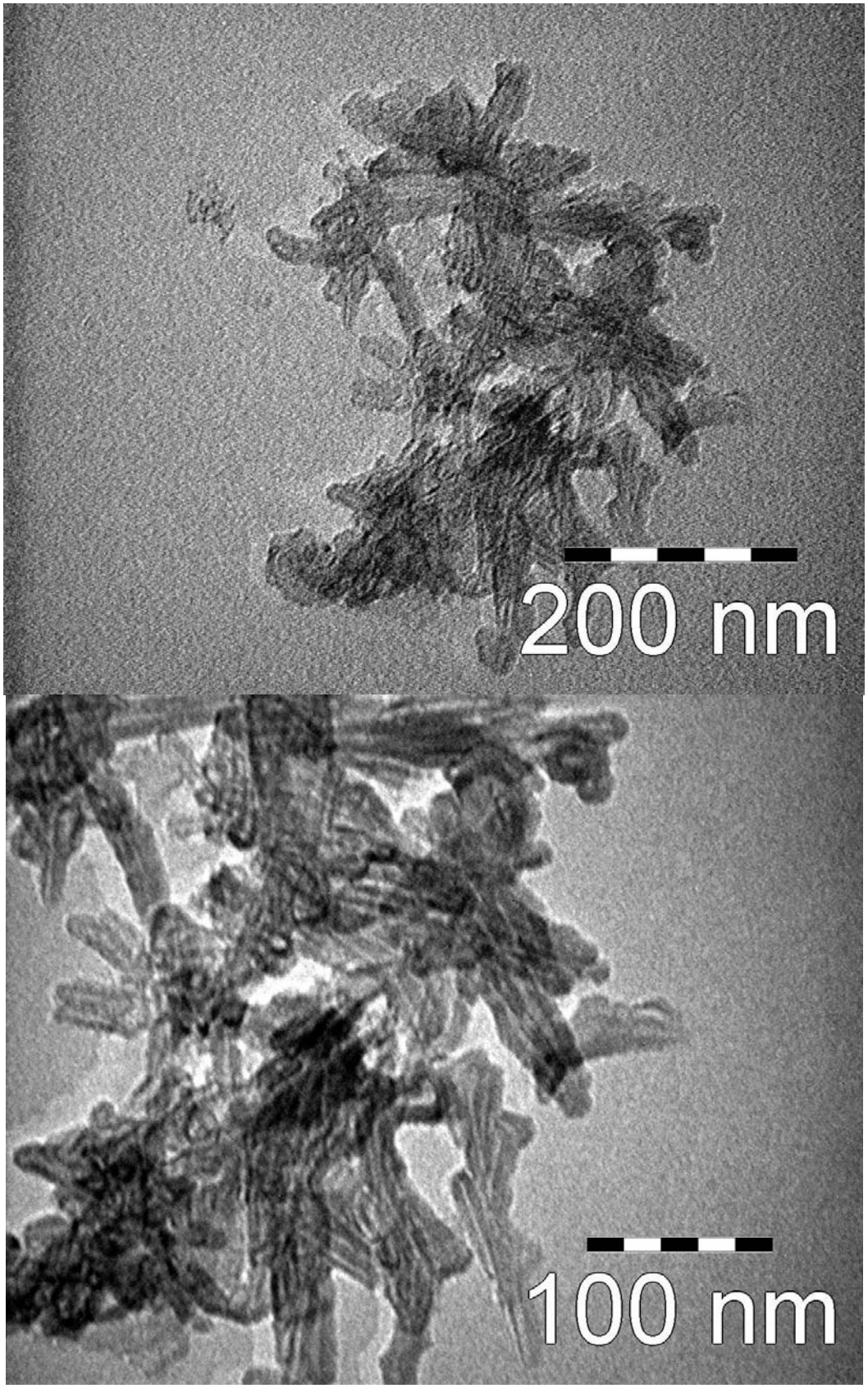
200 nm
100 nm

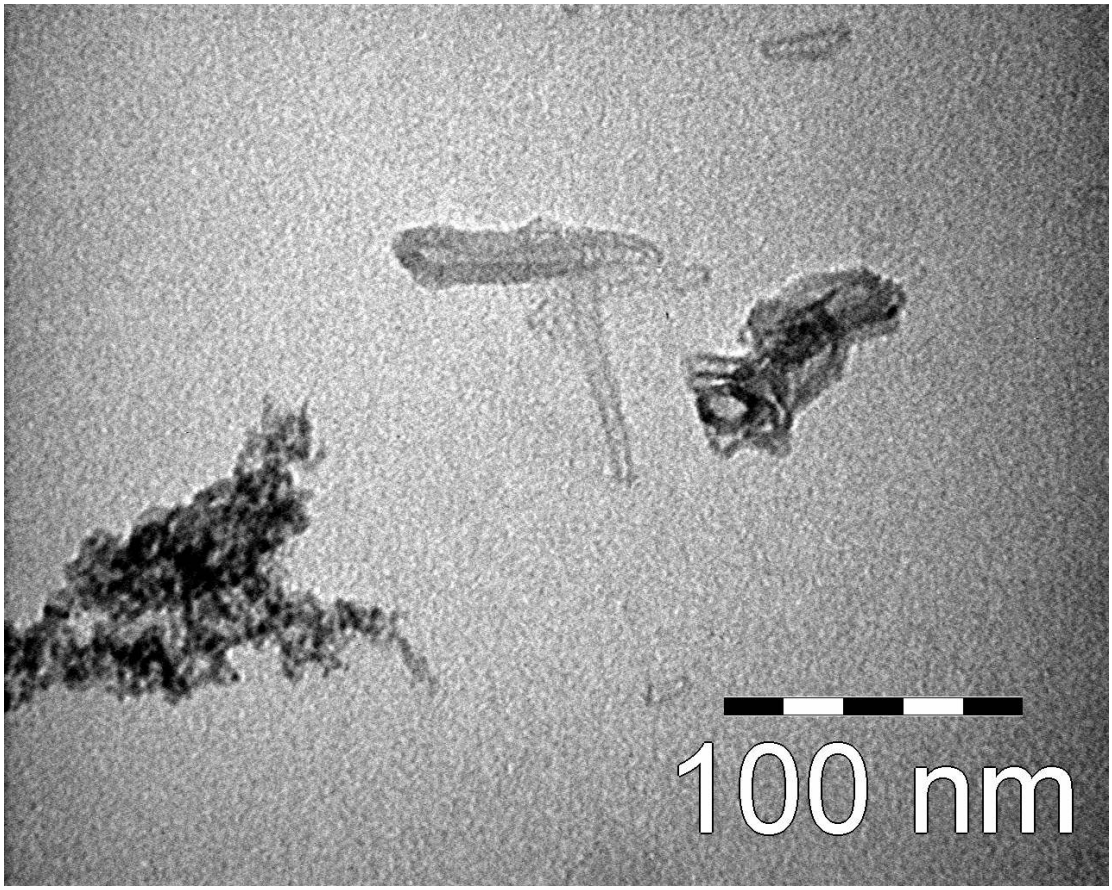

Figure 33 MWNTs observed at 1.2 equivalence ratio

The over-coating of nanotubes can stem from several factors. As described earlier, the nanotube forms by carbon atoms bonding to catalyst particle and propagating in the chain manner. However, excess carbon can deactivate the catalyst which would stop the growth of the nanotube and result in over-coating. In addition, longer residence times can also cause an increase in graphitic content on the surface of the precursor, due to a tempering process[67].

The main question that arises at this point is why C_2H_4 used as fuel facilitates generation of MWNTs, while CH_4 does not. Yet again, the equivalence ratio, ferrocene feeder temperature and gas velocity are kept similar when using both gases.

The first thing that is analyzed is the temperature of the flame. The temperature of the methane flame can be found using SPIN code. STANJAN can be used to find adiabatic flame temperature for both methane and ethylene flame. A thermocouple measurement of the flame temperature is attempted as well, but does not yield reliable results. First of all, insertion of the thermocouple into the flame and subsequent adjustment of vertical position of thermocouple within the flame is extremely problematic with front acrylic gate closed, since one cannot adjust the position from outside. On the other hand, the flame flashes back when the acrylic gate is open. Furthermore, even if the thermocouple is inserted into the flame with the gate closed, the thermocouple disturbs the flame and forces parts of the flame closest to the thermocouple to change position. The main reason for that is quenching, since the temperature of the thermocouple is less than that of the flame. As a result, thermocouple acts as a heat sink for the flame.

Gas	Equivalence Ratio	Adiabatic Flame Temp (K)	Peak Temperature predicted by SPIN (K)
Methane	1.2	1895	1863
Ethylene	1.167	1703	-
Ethylene	1.271	1604	-
Ethylene	1.38	1524	-

Table 4 Comparison of adiabatic flame temperatures for methane and ethylene flame

As we can see in Table 4, the adiabatic flame temperature of the methane flame is very close to the peak temperature predicted by the SPIN simulation; in fact the difference is less than 2%. This indicates that convection and radiation losses that the flame experiences are low enough as to allow us to approximate the temperature of ethylene flame based on the adiabatic temperature.

From Table 4, it is clear that the temperature of the ethylene flame at 1.2 equivalence ratio is 300° C lower than the temperature of methane flame at the same equivalence ratio. The reason is the addition of nitrogen to the ethylene flame in order to prevent the flashback. Addition of nitrogen increases the overall gas speed, but dramatically lowers the temperature.

The methane flame is then diluted with nitrogen as well, with the resulting adiabatic flame temperature ranging from 1620 to 1800 K, with no observed difference in the nanostructure yield.

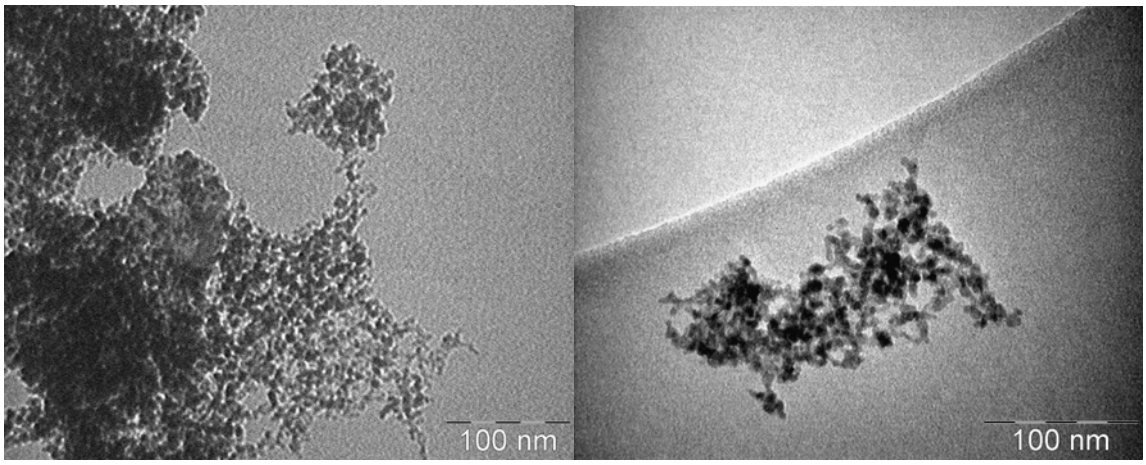

Figure 34 Particles generated using: A-methane flame with adiabatic temperature of 1620 K, B - methane/acetylene flame with adiabatic temperature of 1710 K

As in pictures observed previously, the generated catalyst particles are small enough to facilitate the growth of CNTs. In Fig. 34a, we can see agglomerates of particles held together. However, the image resolution is not high enough as to be able to distinguish if there are CNTs that bond the particles together.

4.4 SWNTs

The presence of SWNTs is mainly identified using Raman spectroscopy, although TEM images also show the areas of possible SWNT existence. It is important to note, however, that HRTEM is necessary for imaging SWNTs but the author of this work had only access to TEM.

	Experimental Peaks (cm^{-1})	Theoretical Peak Range (cm^{-1})
RBM	279	75 - 300
D-band	1372	1250 - 1450
G-band	1582	1500 - 1605

Table 5 Comparison of experimentally obtained and theoretical Raman peaks

The Raman peaks observed in this experiment and illustrated in Table 5 fall well within the range of anticipated values previously found by other researchers[63, 64]. Figure 35 reveals a clear RBM peak at 279 cm^{-1}, which is indicative of SWNT presence. Utilizing the technique proposed by Bandow *et al*[64], we calculate the inner radius of SWNTs to be approximately 0.81 nm. One observed peculiarity is the fact that the RBM mode generally obtained using either 514.5 or 647 nm excitation is centered at 180-190 cm^{-1}. However, the fact that different experimental setups and conditions are used in those experiments can account for the difference, as SWNTs generated under different conditions would have different inner radii, e.g. 1.21 nm in diameter for 185 cm^{-1} peak. This would also make the nanotubes generated in this experiment harder to pinpoint using TEM due to smaller diameter, as we see in Fig. 37.

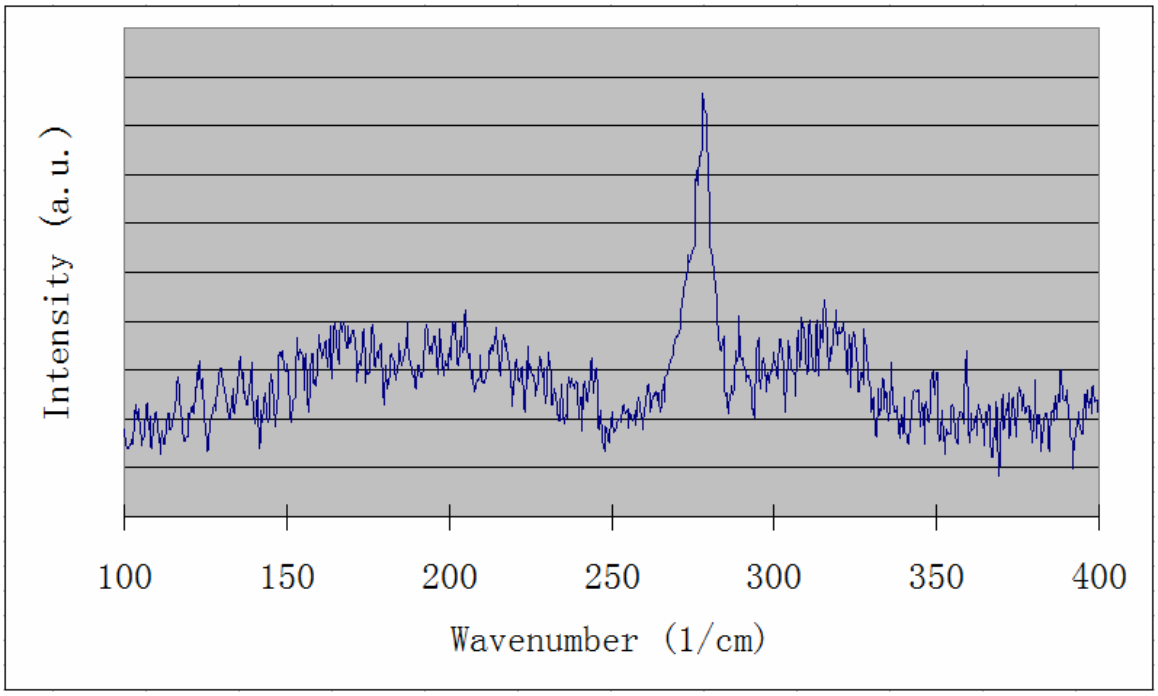

Figure 35 RBM observed using Raman spectroscopy

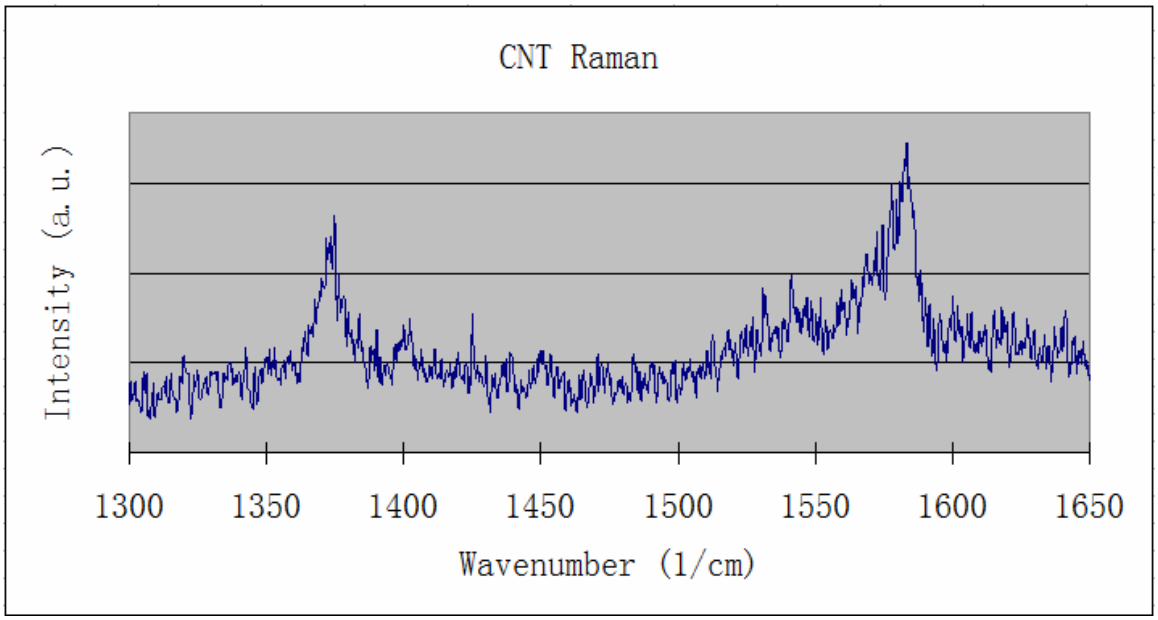

Figure 36 D- and G-band observed using Raman spectroscopy

A well defined G-band at 1582 cm^{-1} is another indication of possible SWNT presence, although no additional information can be extrapolated from its location. The

D-band observed at 1372 nm indicates the presence of amorphous carbon or MWNTs. Both G- and D-band are shown in Fig. 36

The images obtained using TEM only show a possible area for SWNT concentration, but no actual nanotubes. Figure 37 shows an area of changing contrast, which could be indicative of nanotube presence. Further studies utilizing HRTEM are needed to give a definitive answer.

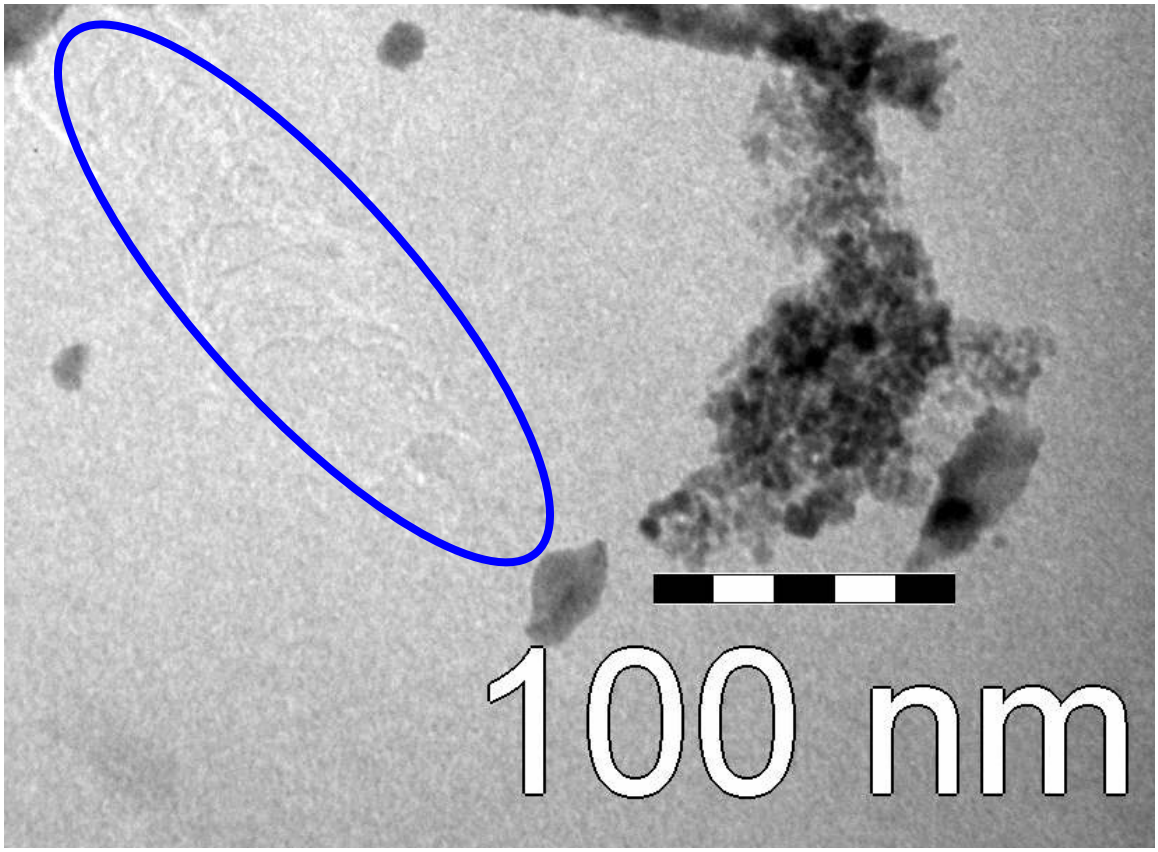

Figure 37 Area of potential SWNT growth observed under TEM

However, difficulties can be encountered even when observing SWNTs under high magnification TEM. As Nasibulin *et al*[55] pointed out, SWNTs can be destroyed very easily when high power electrons bombard them for an extended period of time.

4.5 Simulation and Formation Mechanism

The critical factors for nanotube formation are temperature, velocity, radical presence in the flame and catalyst precursor loading rate. While the velocity can be easily calculated based on MFC settings and the Clausius-Clapeyron equation can be used to find the loading rate, exact temperature of the flame and radical concentration are approximated using numeric simulations. The validity of temperature measurements obtained using the SPIN simulation is demonstrated earlier by comparison with the STANJAN computation of adiabatic flame temperature. The difference of less than 2% indicates that SPIN results may be close to the actual flame parameters.

SPIN simulations are conducted at 1.15, 1.2 and 1.3 equivalence ratios. The flame position matches the simulations exactly at 1.15 and 1.2 equivalence ratios, while the experimental flame at simulation settings for 1.3 equivalence ratio tends to flash back into the burner. The temperatures and velocities of the flames at different equivalence ratios are shown in Fig. 38, 39, and 40.

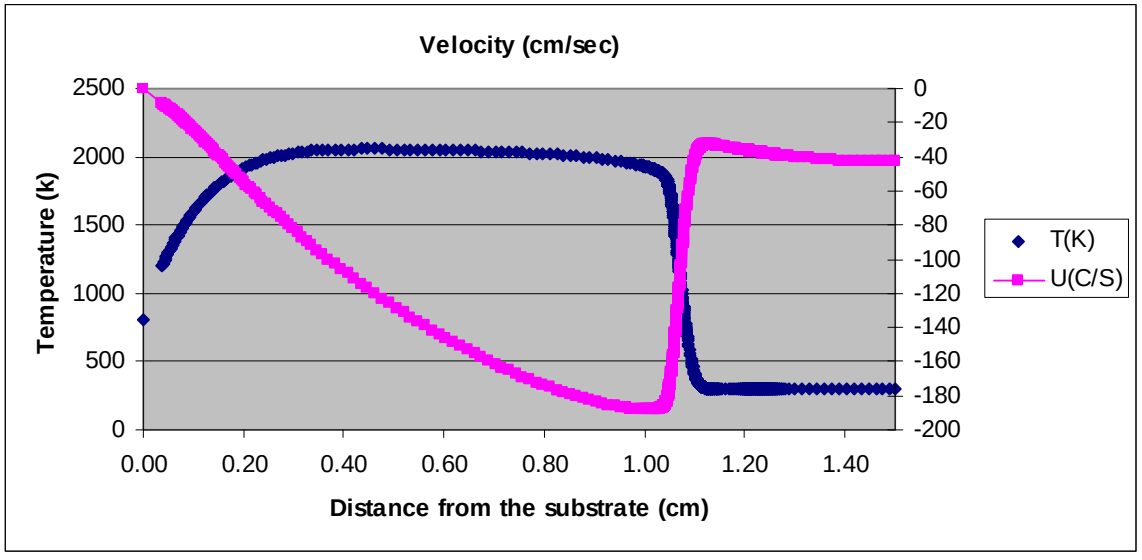

Figure 38 Velocity and temperature at 1.15 equivalence ratio

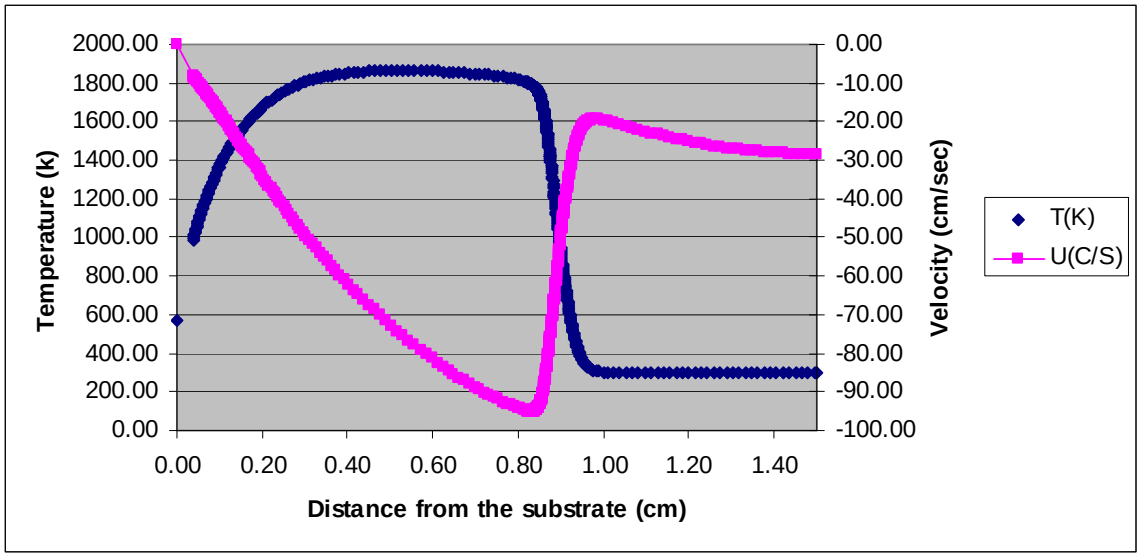

Figure 39 Velocity and temperature at 1.2 equivalence ratio

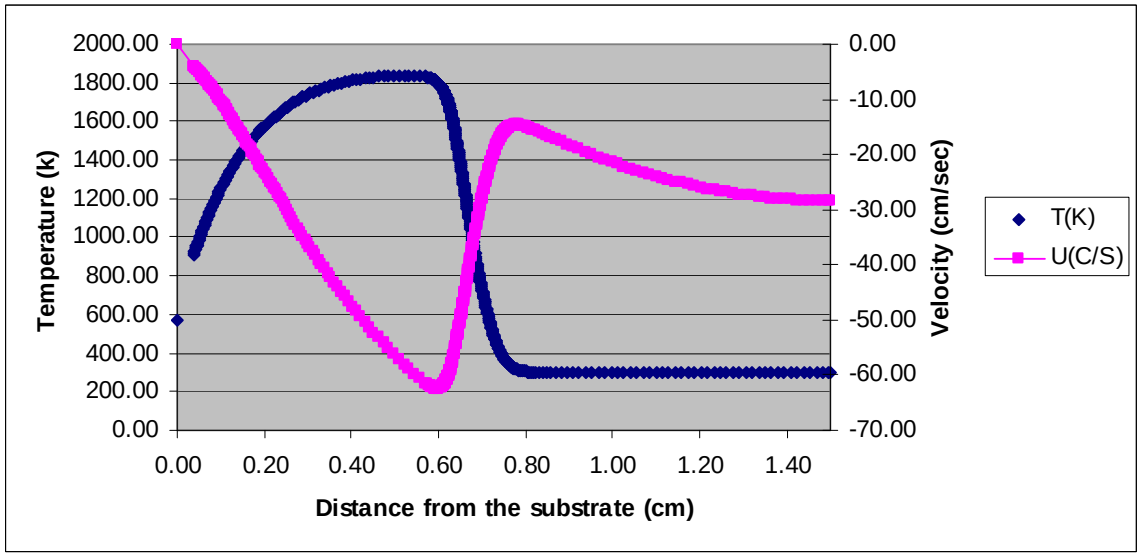

Figure 40 Velocity and temperature at 1.3 equivalence ratio

One can see that in all three obtained simulations, temperatures are strikingly similar. What is different is a velocity for 1.3 equivalence ratio that could possibly account for the flame position difference between that predicted by the simulation and the actual. While the gas velocity at the burner is maintained at about 27 cm/sec, peak velocity for the 1.15 equivalence ratio is 188 cm/sec, which is twice as large as the peak

velocity for 1.2. Velocity for 1.2 equivalence ratio is 95 cm/sec, while it still decreases for the 1.3 equivalence ratio to become 62 cm/sec.

The main implication of the changing peak velocity is its influence on the residence time, which is the time that carbon nanotubes have to form in the flame before reaching the substrate. The residence time is indeed one of the most critical factors influencing nanotube growth. All other parameters being perfect for nanotube growth, insufficient or overly long residence time can have dramatic effect on CNTs. If residence time is too short, the nanotubes will not have enough time to form. On the other hand, if residence time is too long the nanotubes can become over-coated with carbon.

The residence time can be easily found using simple numeric integration of the SPIN results. The area under velocity curve from the flame to the substrate represents the distance an average particle would spend traveling from the flame to the substrate, from which a time can be easily found. Table 6 compares residence times for three experimental settings. The residence time is defined as the time it takes for a particle in the flow to travel from the point of peak velocity to the point 0.08 cm from the substrate. The reason 0.08 cm distance from the substrate is utilized is because the simulation predicts that the flow slows down before reaching the substrate due to the stagnation point flow effects. However, the samples in this experiment are collected on the tungsten wire that is 0.08 cm in diameter, which makes the previous assumption reasonable.

Equivalence Ratio	Residence Time (ms)
1.1	10
1.2	15.2
1.3	18.2

Table 6 Residence time dependence on the equivalence ratio

As we can see, the residence time increases as the equivalence ratio increases, which is expected since velocity decreases with equivalence ratio. It is important to note that the residence time found for 1.3 equivalence ratio case is based on the simulation flame position, which does not agree with the experimental location.

Obtained residence times explain why no CNTs or fibers are obtained below 1.2, with the reason being that residence time is not long enough to allow for CNT formation. Vander Wal *et al*[68] in fact uses metallocenes in diffusion flame synthesis of nanotubes and finds that close to 20 ms is necessary for nanotubes to grow. Thus from the residence time standpoint, the larger equivalence ratio may be preferable for nanotube formation.

Another aspect that has been identified in literature as a critical factor for nanotube formation is CO presence. The importance of the fact is that CO decomposition in the flame, as well as the decomposition of hydrocarbons, is one of the major criteria driving the formation of the nanotubes[54]. Similar to the impact of residence time, too much of available carbon can lead to over-coating and the cessation of nanotube growth, while not enough carbon will not allow the nanotube to grow. In fact, most researchers consider CO to be of such importance that they use it as a carrier gas for the catalyst. In this work, an abundance of CO is generated naturally within the flame due to the high equivalence ratio and N_2 is considered to be an appropriate carrier gas for the precursor catalyst.

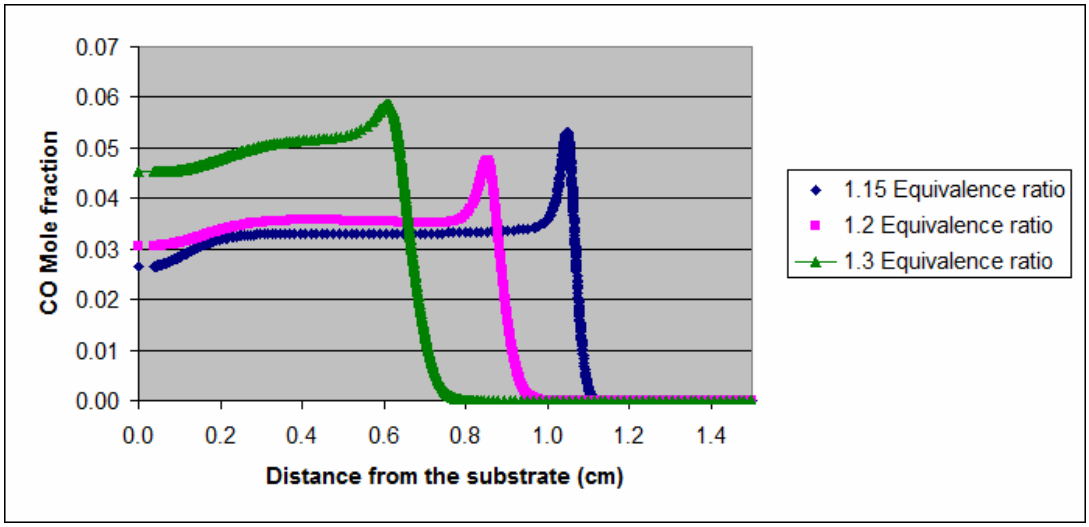

Figure 41 CO concentration comparison between different equivalence ratios

Comparing the CO concentration of 1.15, 1.2, and 1.3 equivalence ratios, a peculiar trend, shown in Fig. 41, emerges. We see the highest CO concentration for 1.3 equivalence ratio, and the lowest for 1.2 equivalence ratio. The reason no CNT growth occurred at 1.15 and 1.3 equivalence ratios might be because even though the CO concentration is high, the residence time or the temperature of the flame is not optimal.

Another element thought to be critical for nanotube formation is H_2. Both Vander Wal *et al*[45, 49] and Nasibulin *et al*[53] observed the dependence of CNT formation on the availability of H_2 in the flame. H_2 is thought to help the dissociation of CO[49], while also facilitating carbon deposition as well as surface catalytic activity[45].

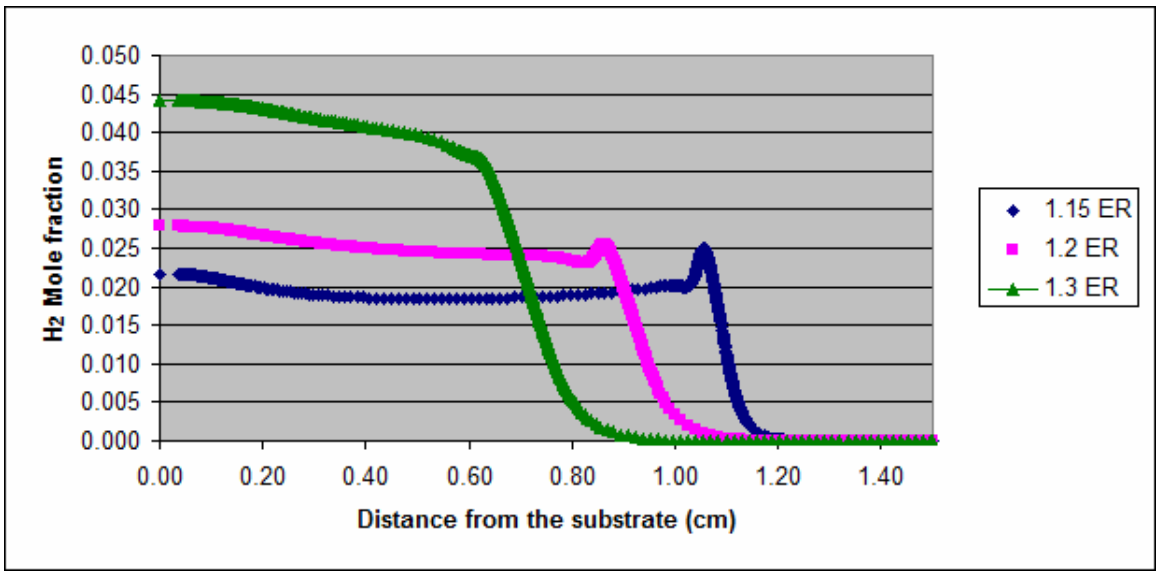

Figure 42 H_2 concentration comparison between different equivalence ratios

Simulation for the observed experimental settings shows that H_2 concentration remains relatively similar for 1.15 and 1.2 equivalence ratios, as can be observed in Fig. 42. However, the concentration increases dramatically for the 1.3 case. Furthermore, the concentration curve from the burner to the substrate for 1.3 equivalence ratio case has a different shape than those for 1.15 and 1.2 cases, which could be due to a change in the flame combustion mechanism.

The role of C_2H_2 radicals on the other hand is not very well understood. While in some experiments addition of C_2H_2 caused particle over-coating with resulting encapsulation and diminishing yield of CNTs[46, 47, 49], Baker *et al*[20] considered C_2H_2 a necessary element for successive carbon diffusion.

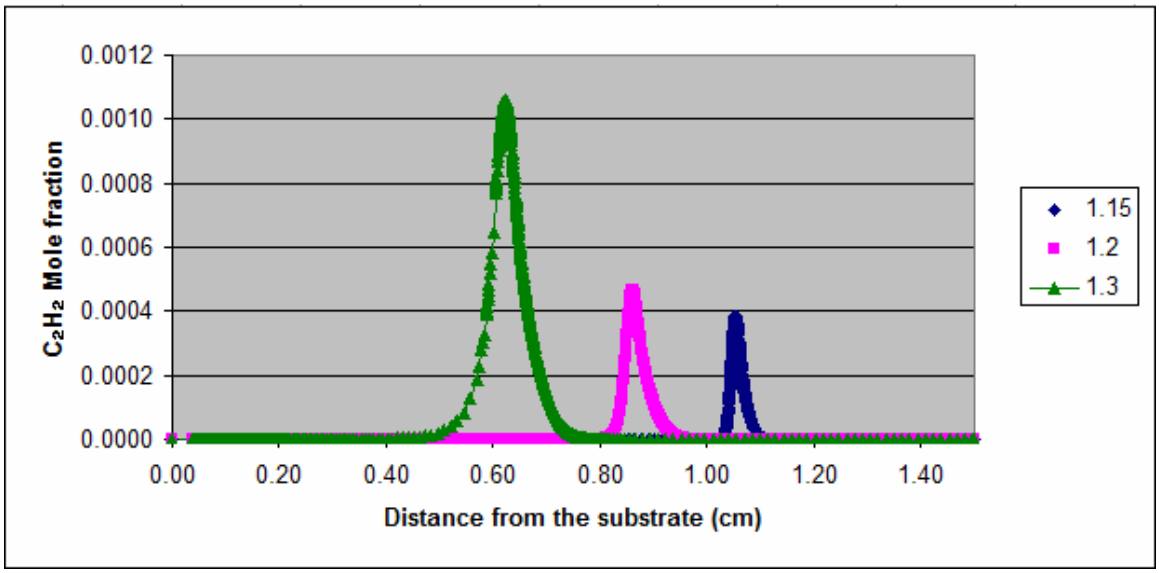

Figure 43 C_2H_2 concentration comparison between different equivalence ratios

Simulation for the C_2H_2, shown in Fig. 43, yields a clear trend that shows concentration increase accompanying an increase of equivalence ratio. Through TEM observations, it is found that particle over-coating increases at higher equivalence ratios, which corresponds with the increase of C_2H_2 mole ratio and agrees with Vander Wal's and Nasibulin's observations discussed earlier.

Chapter 5. Conclusions and Future Work

Premixed methane-air and ethylene-air stagnation point flame with ferrocene catalyst precursor is used to generate nanofibers, MWNTs and SWNTs. The optimal loading rate for the ferrocene addition is experimentally determined, based on initial values found in literature.

Nanofibers and CNTs are collected on a tungsten wire placed on the water-cooled copper substrate located 1.5 cm below the nozzle of the burner. For TEM analysis, wire is ultrasonicated in ethanol, with the solution deposited on the TEM grids.

SEM analysis shows nanofibers synthesized at 1.2 equivalence ratios, while EDS confirms a significant presence of carbon and iron on the analyzed samples. Some nanofibers are synthesized at 1.1 and 1.3 equivalence ratios, while no nanostructures are observed at 1.0 and 1.4 equivalence ratios.

TEM imaging reveals MWNTs generated using ethylene flame at 1.27 equivalence ratio with CNTs that are 5-7 nm in diameter and at least 100 nm in length. However, using methane flames of the same equivalence ratio and flame temperature did not generate nanotubes.

Raman spectroscopy shows distinctive peaks for RBM, D-band, and G-band that identify the presence of SWNTs. TEM imaging reveals areas of possible SWNT agglomeration, while not providing enough resolution for conclusive characterization. HRTEM analysis is needed to characterize SWNTs.

Numerical simulations reveal that CO concentrations for 1.2 equivalence ratios are lower than for that 1.15 and 1.3 equivalence ratios. This could indicate that even though an abundance of CO is present, the temperature might not be optimized to utilize all of

CO available. Computed H_2 concentration for different equivalence ratios is relatively similar for 1.15 and 1.2 equivalence ratios, and thus does not allow drawing any definite conclusions related to H_2 role in formation of CNTs. The simulations show an increasing C_2H_2 concentration from 1.15 to 1.3 equivalence ratios, corresponding to the experimental observations of carbon over-coating of catalyst particles at higher equivalence ratios.

Some of the future work needed to refine the studies discussed in this thesis entails performing HRTEM characterization and conducting more experiments using C_2H_4 as fuel. Experimental settings minimizing over-coating of MWNTs should be found. Additionally, SPIN simulations should be used to determine species concentration and temperature profile in C_2H_4-based flame, which will allow for a better comparison with the CH_4 flame. The role of CO can be better understood if additional CO is added into the flame and its influence on MWNTs is observed.

References

[1] Grobert, N., Carbon nanotubes – becoming clean, *Materials Today* **10**:28–35 (2007)
[2] Monthioux, M., and Kuznetsov, V. L., Who should be given the credit for the discovery of carbon nanotubes?, *Carbon* **44**:1621-1623 (2006)
[3] Iijima, S., Helical microtubles of graphitic carbon, *Lett. to Nature* **354**:56-58 (1991)
[4] Thostenson, E. T., Ren, Z., and Chou, T., Advances in the science and technology of carbon nanotubes and their composites: a review, *Composites Science and Technology* **61**:1899–1912 (2001)
[5] Dai, H., Carbon nanotubes: opportunities and challenges, *Surface Science* **500**:218–241 (2002)
[6] Forró, L., Salvetat, J.-P., Bonard, J-M., Bacsa, R., Thomson, N. H., Garaj, S., Thien-Nga, L., Gaal, R., Kulik, A., Ruzicka, B., Degiorgi, L., Bachtold, A., Schonenberger, C., Pekker, S., and Hernadi, K., Electronic and mechanical properties of carbon nanotubes, in Science and Application of Nanotubes (Tomanek and Enbody, eds), Kluwer Academic/Plenum Publishers, New York, 2000
[7] Daenen, M., de Fouw, R.D., Hamers B., Janssen, P.G.A., Schouteden, K. and Veld, M.A.J., The wondrous world of carbon nanotubes, Eindhoven University of Technology, 2003, http://students.chem.tue.nl/ifp03/Wondrous%20World%20of%20Carbon%20Nanotubes_Final.pdf
[8] Yu, M-F., Lourie, O., Dyer, M. J., Moloni, K., Kelly, T. F., and Ruoff, R. S., Strength and breaking mechanism of multiwalled carbon nanotubes under tensile load, *Science* **287**:637-640 (2000)
[9] Terrones, M., Science and technology of the twenty-first century: synthesis, properties, and applications of carbon nanotubes, *Annu. Rev. Mater.Res*. **33**:419–501 (2003)
[10] Ruoff, R. S., and Lorents, D. C., Mechanical and thermal properties of carbon nanotubes, *Carbon* **33-7**:925-930 (1995)
[11] Baughman, R. H., Zakhidov, A. A., and de Heer, W. A., Carbon nanotubes-the route toward applications, *Science* **297**:787-792 (2002)
[12] Kim, P., Shi, L., Majumdar, A., and McEuen, P. L., Thermal transport measurements of individual multiwalled nanotubes, *Phys. Rev. Lett.* **87-21**:1-4 (2001)
[13] Nikitin, A., Ogasawara, H., Mann, D., Denecke, R., Zhang, Z., Dai, H., Cho, K. J., and Nilsson, A., Hydrogenation of Single-walled Carbon Nanotubes, *Phys. Review Lett*. **95**:225507 (2005)
[14] Popov, V., Carbon nanotubes: properties and applications, *Materials Science and Engineering* **43**:61–102 (2004)
[15] Dai, H., Rinzler, A. G., Nikolaev, P., Thess, A., Colbert, D. T., and Smalley, R. E., Single-wall nanotubes produced by metal-catalyzed disproportionation of carbon monoxide, *Chem. Phys. Lett.* **260**:471-475 (1996)
[16] Nikolaev, P., Bronikowski, M. J., Bradley, R. K., Rohmund, F., Colbert, D. T., Smith, K. A., and Smalley, R. E., Gas-phase catalytic growth of single-walled carbon nanotubes from carbon monoxide, *Chem. Phys. Lett.* **313**:91–97 (1999)
[17] Bucky Balls, Fullerenes, and the Future: An Oral History Interview with Professor Richard E. Smalley January 22, 2000, http://www.davis-

floyd.com/USERIMAGES/File/Bucky%20balls%20Fullereness%20and%20the%20futur e.pdf
[18] Vander Wal, R. L., and Hall L. J., Flame synthesis of Fe catalyzed single-walled carbon nanotubes and Ni catalyzed nanofibers: growth mechanisms and consequences, *Chem. Phys. Lett.* **349**:178-184 (2001)
[19] Rodriguez, N. M., A review of catalytically grown carbon nanofibers, *J. Mater. Res*. **8-12**:3233-3250 (1993)
[20] Baker, R. T. K., Barber, M. A., Harris, P. S., Feates, F. S., and Waite, R. J., Nucleation and growth of carbon deposits from the nickel catalyzed decomposition of acetylene, *JOURNAL OF CATALYSIS* **26**:51-62 (1972)
[21] Moisala, A., Nasibulin, A.G., and Kauppinen, E.I., The role of metal nanoparticles in the catalytic production of single-walled carbon nanotubes – a review, *J. Phys.: Condens. Matter* **15**:3011-3035 (2003)
[22] Sinnott, S. B., Andrews, R., Qian, D., Rao, A. M., Mao, Z., Dickey, E. C., and Derbyshire, F., Model of carbon nanotube growth through chemical vapor deposition, *Chem. Phys. Lett.* **315**:25–30 (1999)
[23] Hutchison, J. L., Kiselev, N. A., Krinichnaya, E. P., Krestinin, A. V., Loutfy, R. O, Morawsky, A. P., Muradyan, V. E., Obraztsova, E. D., Sloan, J., Terekhov, S. V., and Zakharov, D. N., Double-walled carbon nanotubes fabricated by a hydrogen arc discharge method, *Carbon* **39**:761–770 (2001)
[24] Jung, S. H., Kim, M. R., Jeong, S. H., Kim, S. U., Lee, O. J., Suh, J. H., and Park, C. K., High-yield synthesis of multi-walled carbon nanotubes by arc discharge in liquid nitrogen, *Appl. Phys. A.* **76**:285–286 (2003)
[25] Lee, S. J., Baik, H. K., Yoo, J., and Han, J. H., Large scale synthesis of carbon nanotubes by plasma rotating arc discharge technique, *Diamond and Related Materials* **11**:914–917 (2002)
[26] Zhang, Y., and Iijima, S., Formation of single-wall carbon nanotubes by laser ablation of fullerenes at low temperature**,** *Appl. Phys. Lett.* **75-20**:3087-3089 (1999)
[27] Scott, C. D., Arepalli, S., Nikolaev, P., and Smaley, R. E., Growth mechanisms for single-wall carbon nanotubes in a laser-ablation process**,** *Appl. Phys. A.* **72**:573–580 (2001)
[28] Halstead, B. W., Brack, N.,Rider, A. N., Yeo, E., Pigram, P. J., Glaisher R., and McCulloch, D. G., Scaled-up production of multi-walled carbon nanotubes using catalytic chemical vapour deposition, Nanoscience and Nanotechnology, ICONN 2006, http://ieeexplore.ieee.org/iel5/4143299/4140639/04143352.pdf?tp=&isnumber=&arnumb er=4143352
[29] Zhang, Z. J., Wei, B. Q., Ramanath, G., and Ajayan, P. M., Substrate-site selective growth of aligned carbon nanotubes, *Applied Physics Letters* **77-23**:3764-3766 (2002)
[30] Fan, S., Chapline, M. G., Franklin, N. R., Tombler, T. W., Cassell, A. M., and Dai, H., Self-oriented regular arrays of carbon nanotubes and their field emission properties, *Science* **283**:512-514 (1999)
[31] Che, G., Lakshmi, B. B., Martin, C. R., and Fisher, E. R., Chemical vapor deposition based synthesis of carbon nanotubes and nanofibers using a template method, *Chem. Mater* **10**:260-267 (1998)
[32] Height, M. J., Howard, J. B., and Tester, J. W., Flame synthesis of single-walled carbon nanotubes, *Proceedings of the Combustion Institute* **30**:2537–2543 (2005)

[33] Vander Wal, R. L., Berger, G. M., and Ticich, T. M., Flame synthesis of single-walled carbon nanotubes and nanofibers, NASA/CP—2003-212376 *http://ntrs.nasa.gov/archive/nasa/casi.ntrs.nasa.gov/20040053544_2004055210.pdf*
[34] Kennedy, L. A., Carbon nanotubes, synthesis, growth and orientation control in opposed flow diffusion flames, *Journal of Heat Transfer* **130**:042402-1-11 (2008)
[35] Yuan, L., Saito, K., Pan, C., Williams, F. A., and Gordon, A. S., Nanotubes from methane flames, *Chem. Phys. Lett.* **340**:237-241 (2001).
[36] Yuan, L., Saito, K., Hu, W., and Chen, Z., Ethylene flame synthesis of well aligned multi-walled carbon nanotubes, *Chem. Phys. Lett.* **346**:23-28, 2001
[37] Yuan, L., Li, T., and Saito, K., Growth mechanism of carbon nanotubes in methane diffusion flames, *Carbon* **41**:1889–1896 (2003)
[38] Vander Wal, R. L., Flame synthesis of substrate-supported metal-catalyzed carbon nanotubes, *Chem. Phys. Lett.* **324**:217–223 (2000)
[39] Lee, G.W., Jurng, J., and Hwang, J., Formation of Ni-catalyzed multiwalled carbon nanotubes and nanofibers on a substrate using an ethylene inverse diffusion flame, *Combust Flame* **139**:167–75 (2004)
[40] Merchan-Merchan, W., Saveliev, A., Kennedy, L. A., and Fridman, A., Formation of carbon nanotubes in counter-flow, oxy-methane diffusion flames without catalysts. *Chem. Phys. Lett*. **354:**20-24 (2002)
[41] Diener, M. D., Nichelson, N., and Alford, J. M., Synthesis of single-walled carbon nanotubes in flames. *J.Phys. Chem. B* **104-41**:9615–9620 (2000)
[42] Duan, H. M., and Mc Kinnon, J. T., Nanoclusters produced in flames. *J. Phys Chem.* **98-49**:12815-12818 (1994)
[43] Chowdhury, K. D., Howard, J. B., and Vander Sande, J. B., Fullerenic Nanostructures in Flames., *J. Mater. Res*. **11-2**:341–347 (1996)
[44] Goel, A., Hebgen, P., Vander Sande, J. B., and Howard, J. B., Combustion synthesis of fullerenes and fullerenic nanostructures, *Carbon* **40**:177–182 (2002)
[45] Vander Wal, R. L., Hall, L. J., and Berger, G. M., Optimization of flame synthesis for carbon nanotubes using supported catalyst. *J. Phys. Chem*. **106**:13122–13132 (2002)
[46] Vander Wal, R. L., and Hall, L. J., Ferrocene as a precursor reagent for metal-catalyzed carbon nanotubes: competing effects, *Combustion and. Flame* **130**:27–36 (2002)
[47] Vander Wal, R. L. and Ticich, T. M., Flame and furnace synthesis of single-walled and multi-walled carbon nanotubes and nanofibers. *J. Phys. Chem. B* **105**:10249–10256 (2001)
[48] Perla, S., Flame synthesis of carbon-nanostructures, Louisiana State University Electronic Thesis and Dissertation Collection, 2002, Osmania University, 2005, http://etd.lsu.edu/docs/available/etd-11152005-135439/
[49] Vander Wal, R. L., Fe-catalyzed single-walled carbon nanotube synthesis within a flame environment, *Combustion and Flame* **130**:37–47 (2002)
[50] Vander Wal, R. L., and Ticich, T. M., Comparative flame and furnace synthesis of single-walled carbon nanotubes. *Chem. Phys. Lett.* **336**:24-32 (2001)
[51] Murr, L.E., Bang, J. J., Esquivel, E. V., Guerrero P. A., and Lopez, D. A., Carbon nanotubes, nanocrystal forms, and complex nanoparticle aggregates in common fuel-gas combustion sources and the ambient air, *Journal of Nanoparticle Research* **6**:241–251 (2004)

[52] Zhao, B., Uchikawa, K., McCormick, J. R., Ni, C. Y., Chen, J. G., and Wang, H., Ultrafine anatase TiO_2 nanoparticles produced in premixed ethylene stagnation flame at 1 atm, *Proceedings of the Combustion Institute* **30-2**:2569-2576 (2005)
[53] Nasibulin, A. G., Moisala, A., Brown, D. P., Jiang, H., and. Kauppinen, E. I., A novel aerosol method for single walled carbon nanotube synthesis, *Chem. Phys. Lett.* **402**:227–232 (2005)
[54] Moisala, A., Nasibulin, A. G., Shandakov, S. D., Jiang, H., and Kauppinen, E. I., On-line detection of single-walled carbon nanotube formation during aerosol synthesis methods *Carbon* **43**:2066–2074 (2005)
[55] Nasibulin, A. G., Moisala, A., Brown, D. P. and Kauppinen, E. I., Carbon nanotubes and onions from carbon monoxide using $Ni(acac)_2$ and $Cu(acac)_2$ as catalyst precursors, *Carbon* **41**:2711-2724 (2003)
[56] Rozenchan, G., Zhu, D. L., Law, C. K., and Tse, S. D., Outward propagation, burning velocities, and chemical effects of methane flames up to 60 atm, *Proceedings of the Combustion Institute* **29**:1461–1469 (2002)
[57] Li, Y., Hatakeyama, R., Kaneko, T., and Okada, T., Nano sized magnetic particles with diameters less than 1 nm encapsulated in single-walled carbon nanotubes, *Jpn. J. Appl. Phys* **45**:428-431 (2006)
[58] Emel'yanenko, V. N., Verevkin, S. P., Krol, O. V., Varushchenko, R. M., and Chelovskaya, N. V., Vapour pressures and enthalpies of vaporization of a series of the ferrocene derivatives, J. Chem. Thermodynamics **39**:594–601 (2007)
[59] Stone, R., Clarke, A., and Beckwith, P., Correlations for the laminar-burning velocity of methane/diluent/air mixtures obtained in free-fall experiments, *Combustion and Flame* **114**:546–555 (1998)
[60] Richter, H., Howard, J. B., and Vander Sande, J. B., From academic soot research to commercial synthesis of single-walled carbon nanotubes, *American Institute of Chemical Engineers (AIChE) 2005 Annual Meeting: Conference Proceedings*, http://www3.interscience.wiley.com/journal/114192162/abstract?CRETRY=1&SRETRY=0
[61] Pimenta, M. A.,Marucci, A., Brown, S. D. M., Matthews, M. J., Rao, A. M., Eklund, P. C., Smalley, R. E., Dresselhaus, G., and Dresselhaus, M. S., Resonant Raman effect in single-wall carbon nanotubes, *J. Mater. Res.* **13-9**:2396 -2404 (1998)
[62] Dresselhaus, M. S., Dresselhaus, G., Jorio, A., Souza Filho, A. G., and Saito, R., Raman spectroscopy on isolated single wall carbon nanotubes *Carbon* **40**:2043–2061 (2002)
[63] Rao, A. M., Richter, E., Bandow, S., Chase, B., Eklund, P. C., Williams, K. A., Fang, S., Subbaswamy, K. R., Menon, M., Thess, A., Smalley, R. E., Dresselhaus, G., and Dresselhaus, M. S., Diameter-Selective Raman Scattering from Vibrational Modes in Carbon Nanotubes**,** *Science* **275:**187-191 (1997)
[64] Bandow, S., and Asaka, S., Effects of the growth temperature on the diameter distribution and chirality of single-wall carbon nanotubes, *Phys. Rev. Lett.* **80-17**:3779-3782
[65] Hinkov, I., Farhat, S., and Scott, C. D., Influence of the gas pressure on single-wall carbon nanotube formation, *Carbon* **43**:2453–2462 (2005)
[66] Tian, K., Bergmann, U., and Atakan, B., Mass Spectrometric Investigations of the Influence of Ferrocene in a Laminar Premixed Propene Flame and Comparison to

Numerical Modelling, Third European Combustion Meeting ECM 2007, http://www.combustioninstitute.gr/ECM2007/ECM2007forms/FinalProgram.pdf
[67] Grieco, W. J.,Fullerenes and carbon nanostructures formation in flames, 1998, Massachusetts Institute of Technology, 1999, http://hdl.handle.net/1721.1/9654
[68] Vander Wal, R. L., Ticich, T. M., and Curtis, V. E., Diffusion flame synthesis of single-walled carbon nanotubes, *Chem. Phys. Lett.* **323**:217-223 (2000)
[69] Kee, R. J., Grcar, J. F., Smooke, M. D., Miller, J. A., and Meeks, E., PREMIX: A FORTRAN program for modeling steady laminar one-dimensional premixed flames, Sandia National Laboratories, 1985
[70] Coltrin, M. E., Kee, R. J., Evans, G. H., Meeks, E., Rupley, F. M., Grcar, J. F., SPIN a program for modeling one-dimensional rotating-disk / stagnation-flow chemical vapor deposition reactors, Sandia National Laboratories, 1991

Appendix

Sample MFCs Settings for Methane, Ethylene and Methane-Acetylene Flame

	Methane	Nitrogen	Carrier Nitrogen	Nitrogen	AIR
Mass Flow Controller #	1	2	4	6	3
SLMP	2	2	0.02	10	10
MFCs Percent Open	30.00%	40.00%	1.98%	15%	34.61%

	Ethylene	Nitrogen	Carrier Nitrogen	Nitrogen	AIR
Mass Flow Controller #	1	2	4	6	3
SLMP	2	2	1	10	10
MFCs Percent Open	30.56%	85.00%	2.00%	15%	30.00%

	Methane	Acetylene	Nitrogen	Carrier Nitrogen	Nitrogen Co-flow	AIR
Mass Flow Controller #	1	5	2	4	6	3
SLMP	2	0.1	2	0.02	10	10
MFCs Percent Open	29.00%	21.75%	45.05%	1.98%	15%	26.76%

Sample SPIN Input File

```
RSTR
/COMP
FLUX
TRCE
REOR
ENRG
JJRG 400
NMAX 2000
/NADP 1
/NONR
/GFAC 0.1
/TGIV
/OMEG    1000
/SPOS 1.E-9
STAG
/UINF    100.0
/FLAM    1.0 1500.0
TDSK    570.0
TINF    300.0
NPTS      21
XEND     1.5
PRES     1.0
/TOFF
GRAD     0.50
CURV     0.50
REAC     CH4               0.7
REAC     O2                1.167
REAC     N2                5.65
PROD     CO2               0.1
PROD     N2                0.4
PROD     H2O               0.2
ATOL  1.E-7
RTOL  1.E-4
ATIM  1.E-7
RTIM  1.E-2
PRNT    1
/NADP    4
XCEN   0.7
WMIX   1.4
TIME  100  1.0E-5
TIM2  100  1.0E-5
/SFLR    -1.0E-3
TEMP  0.0 970.
TEMP  0.1 1479.
TEMP  0.2 1770.
TEMP  0.3 1910.
TEMP  0.4 1980.
TEMP  0.5 2010.
TEMP  0.6 2015.
TEMP  0.7 2015.
TEMP  0.8 2010.
TEMP  0.9 2005.
TEMP  1.0 2002.
```

```
TEMP  1.1 2000.
TEMP  1.2 1980.
TEMP  1.3 1940.
TEMP  1.4 850.
TEMP  1.5 300.
/UINF  125
/END
UINF    28.4
END
```